



1 **Forearc crustal faulting and estimated worst-case**  
2 **tsunami scenario in the upper plate of subduction**  
3 **zones. Case study of the Morne Piton Fault system**  
4 **(Lesser Antilles, Guadeloupe Archipelago).**

5 Melody Philippon<sup>1,\*</sup>, Jean Roger<sup>2</sup>, Jean-Frederic. Lebrun<sup>1</sup>, Isabelle Thinon<sup>3</sup>, Océane Foix<sup>4</sup>,  
6 Stéphane Mazzotti<sup>4</sup>, Marc-Anadre Gutscher<sup>5</sup>, Leny Montheil<sup>4</sup>, Jean-Jacques Cornée<sup>4</sup>.

7 1. *Géosciences Montpellier, Université de Montpellier, CNRS, Université des Antilles, Pointe-*  
8 *à-Pitre, French West Indies.*

9 2. *Earth and Structure Processes Department, GNS Sciences, Lower Hutt, New Zealand.*

10 3. *BRGM – French Geological survey, 3 avenue Claude Guillemin 45060 Orléans*

11 4. *Géosciences Montpellier, Université de Montpellier, CNRS, Université des Antilles,*  
12 *Montpellier, France.*

13 5. *Geo-Ocean, Univ.Brest, CNRS, Ifremer, Brest, France.*

14 \* *Corresponding author : melody.philippon@univ-antilles.fr*

15

16 **Abstract**

17 In this study, alternatively to the megathrust, we identify upper plate normal faults  
18 orthogonal to the trench as a possible tsunami source along the Lesser Antilles  
19 subduction zone. We study the Morne Piton Fault system, a trench-perpendicular upper  
20 crustal fault affecting the Lesser Antilles forearc at the latitude of Guadeloupe. By the  
21 means of seismic reflection, high resolution bathymetry, Remotely Operated Vehicle  
22 images and dating, we reassess the slip rate of the Morne Piton Fault at  $0.2 \text{ mm.yr}^{-1}$  since  
23 fault inception (*i.e.* 7 Ma), dividing by five previous estimations and thus increasing the  
24 earthquake time recurrence and lowering the associated hazard. We evidence a metric  
25 scarp with striae at the toe of the Morne Piton Fault system suggesting a recent fault  
26 rupture. We estimate a fault rupture area of  $\sim 450\text{-}675 \text{ km}^2$  and then a magnitude range  
27 for the seismic event around  $M_w 6.5 \pm 0.5$ . We present results from a multi-segment  
28 tsunami model representative for the worst-case scenario which gives an overview of  
29 what could happen in terms of tsunami generation if the whole identified Morne Piton  
30 Fault segments ruptured together. Our model illustrates the potential impact of local  
31 tsunamis on the surrounding coastal area as well as local bathymetric controls on



32 tsunami propagation as (i) shallow water plateaus act as secondary sources and are  
33 responsible for a wrapping of the tsunami waves around the island of Marie-Galante, (ii)  
34 canyons are focusing and enhancing the wave height in front of the most touristic and  
35 populated town of the island, (iii) a resonance phenomenon is observed within Les  
36 Saintes archipelago showing that the waves' frequency content is able to perturbate the  
37 sea-level during many hours after the seismic rupture.

38

39 Keywords: subduction zone, forearc, crustal fault, slip rate, tsunami hazard, Lesser  
40 Antilles, Guadeloupe Island

41

## 42 **1. Introduction**

43

44 Regions at the vicinity of active subduction zones are prone to seismic and related  
45 hazards, including tsunamis, exposing their inhabitants to multiple threats. Megathrust  
46 earthquakes represent the greatest threat with the highest seismic moments and  
47 consequently huge tsunamigenic potential (Satake and Tanioka, 1999). Earthquakes  
48 triggered on crustal faults in the overriding plate represent an additional hazard that  
49 needs to be quantified (Bilek, 2010). In order to assess the hazards and mitigate the risks  
50 associated with these crustal faults, it is essential to estimate their slip rates.

51 On land, slip rates on active faults are determined from paleo-seismic trenches (McCalpin,  
52 1996), high resolution geophysical investigation (Wallace, 1981; Zhang et al., 2014),  
53 satellite imagery (Tronin, 2009), InSAR (Biggs and Wright, 2020), geodetic measurement  
54 (GNSS: Smithe et al., 2013) as well as seismicity which account for the present-day strain  
55 accumulation of the crust. Offshore, slip rate estimates are provided by the means of  
56 underwater geodesy (*i.e.* acoustic geodesy: Kido et al., 2006; Petersen et al., 2019; Fujita  
57 et al., 2006) or fiber optic monitoring (Hirata et al., 2002; Gutscher et al., 2019). Event  
58 time recurrence may be estimated by the study of turbidite deposits cores (Cascades:  
59 Goldfinger et al., 2012; Taiwan: Lehu et al., 2016; Antilles: Seibert et al., 2016; New  
60 Zealand: Lewis et al., 1980), high resolution marine seismic and multibeam echo-sounder  
61 data (Escartin et al., 2016, 2018), and submarine dives survey (Geli et al., 2011). However,  
62 constraining hazard models in areas undergoing slow strain rates remains challenging as  
63 the earthquakes recurrence time overcomes the historical period. Indeed, geodetic  
64 measurements require decades-long time series as the resolution of the method is not



65 accurate enough and erosion or high sedimentation rates may have erased or covered,  
66 respectively, the active fault scarps making it difficult to identify active faults segments.  
67 Therefore, datasets based on the last ten to hundred years of record along tectonic  
68 systems undergoing slow strain rates may not be representative of the bulk strain and  
69 may be at the origin of biased estimations of slip rate along these faults.  
70 The Lesser Antilles (Eastern Caribbean) records slow deformation rates as the north and  
71 south American tectonic plates slowly subduct under the Caribbean plate (Figure 1).  
72 Extensional tectonics and normal faulting affect the forearc (Feuillet et al 2002, De Min et  
73 al. 2015, Boucard et al. 2021) but available historical data do not report tsunami events  
74 related to forearc fault rupture. However, the Les Saintes Mw6.3 earthquake of December  
75 2004 ruptured the Roseau normal fault (Feuillet et al. 2011a, Bazin et al. 2010). The  
76 earthquake reached an intensity up to VIII in the Guadeloupe Archipelago (Figure 1),  
77 being felt by most of its 400,000 inhabitants, and was responsible for one casualty. This  
78 earthquake triggered a tsunami with up to 2m high waves at the coast and a maximum  
79 measured run-up distance of 42 m (Zahibo et al. 2005; Le Friant et al. 2008; Cordrie et al.  
80 2020). Prior to this event, this fault was unmapped and therefore not identified as an  
81 active fault (Terrier and Combes 2002). Forearc normal faults, similar to Les Saintes fault  
82 system, may pose a threat to the 4 million inhabitants of the Lesser Antilles that are living  
83 on 17 volcanic arc islands facing the subduction trench to the east and literally sitting  
84 over the subduction interface.  
85 The present study focuses on the Morne Piton Fault system, perpendicular to the  
86 subduction trench, which is one of the most prominent onshore-offshore fault systems  
87 which cuts the Guadeloupe Archipelago arc and forearc islands (Figure 1). Regarding the  
88 seismic and tsunami hazards related to this fault system and the vulnerability of the  
89 coastal population and infrastructures of the archipelago, the objectives are to (1)  
90 estimate the fault slip rate (2) determine the geometry of the fault segments, and (3)  
91 model the associated tsunami hazard, since such a joint approach has been lacking so far.  
92 In the following study, the fault geometry is refined in order to provide an up-to-date map  
93 of the fault segments thanks to high-resolution (HR) bathymetric data. Then, we integrate  
94 its long-term slip rate over the last *ca.* 7 My, *i.e.* from fault initiation to present-day, by the  
95 mean of HR seismic reflection lines and available or recent biostratigraphic and isotopic  
96 dates. Secondly, Remotely Operated Vehicles (ROV) explorations of seafloor rupture  
97 allowed us to measure the height of the fault scarp and to determine the fault kinematics



98 from striations corresponding to the most recent earthquakes. The overall geometry of  
99 this fault system is comparable to the Les Saintes fault system in terms of length, seafloor  
100 scarp and dip. We thus postulate that a rupture along the Morne Piton Fault may trigger  
101 a local tsunami, close to the coasts of the Guadeloupe Archipelago. Then, we assess the  
102 seismogenic and tsunamigenic potential of the Morne Piton Fault system providing an  
103 overview of what could happen in terms of tsunami generation if all the segments of the  
104 Morne Piton Fault ruptured simultaneously, *i.e.* a plausible worst-case scenario. We  
105 further discuss the local bathymetric controls on the propagation of the ensuing tsunami  
106 wave and the consequences (*e.g.* amplifications and interferences) in near-shore areas of  
107 the neighboring highly populated islands. Finally, we reassess the importance of forearc  
108 crustal faults as potential major tsunami sources in subduction zones worldwide.

109

## 110 **2. Geological settings**

111 Oceanic lithosphere of the North and South American plates is slowly subducting  
112 beneath the Caribbean plate at a convergence rate of  $\sim 2\text{cm.yr}^{-1}$  (Figure 1, DeMets et al.,  
113 2000; Feuillet et al., 2001; Philippon and Corti, 2016). The convex trench geometry  
114 results in along strike variations of obliquity, increasing northward from Guadeloupe.  
115 Along the arc, at the latitude of Guadeloupe, oblique subduction is accommodated by  
116 trench-parallel left-lateral strike slip faults such as the Montserrat-Bouillante / Les  
117 Saintes corridor (located within the volcanic arc), the Bunce fault (located along the  
118 crustal buttress), and a series of trench-perpendicular grabens forming a sinistral  
119 horsetail (Feuillet et al., 2002; Feuillet et al 2010; Ten Brink et al., 2004; Laurencin et al.,  
120 2019; Boucar et al., 2021) (Figure 1, Figure 2A).

121 In the central Lesser Antilles, the Marie-Galante Basin (Guadeloupe Archipelago),  
122 is located at the southern end of the aforementioned regional horsetail system and is  
123 described as a conjugated normal fault system defining a trench perpendicular graben  
124 (Figure 2 A; Feuillet et al., 2001, 2011). This graben affects sediment deposits comprising  
125 three regional mega-sequences: an Eocene(?) - Early Miocene MG-MS1 sequence, a mid-  
126 Miocene - late Tortonian / early Messinian MG-MS2 sequence, and a Messinian to present  
127 MG-MS3 sequence (Bouysse et Mascle 1994; De Min 2014; De Min et al., 2015; Cornée et  
128 al 2023). It shapes the Marie-Galante Basin (up to 1200 m water depth) and  
129 surroundings, Grande Terre and Marie-Galante Islands, respectively (Figure 1). The  
130 northern boundary of the Marie-Galante Basin is the east trending, south dipping Gosier



131 fault that runs primarily onshore along the southern coast of Grande-Terre (Garrabé and  
132 Andreieff, 1988; and Figure 2A). The southern boundary of the basin consists of the  
133 N100° trending, ~50 km-long, north dipping Morne Piton Fault, which crosscuts the  
134 northern edge of Marie-Galante Island (Bouysse et al., 1993) and extends offshore on both  
135 sides of the island (Feuillet et al., 2002, 2004).

136 The Morne Piton Fault system consists of five main 5-15 km-long segments  
137 trending N90°E ± 30° separated by N140°E shorter right-lateral relays (Figure 2). The  
138 fault scarp is exposed at Anse Piton, eastern coast of Marie-Galante, and shows dip-slip  
139 striations (Feuillet et al., 2002). Onshore Marie-Galante, the fault offsets the Pliocene to  
140 middle Pleistocene platform by ~60 m. It also crosscuts a series of 3 uplifted late-mid to  
141 late Pleistocene terraces along the eastern side of the island. Feuillet et al. (2004)  
142 calculated a 5 km dislocation depth and a 70 to 80°N fault dip to model the observed  
143 flexure of the footwall. Considering that the Marie-Galante Plateau is a flat abandoned  
144 330 Ka old marine terrace, these authors estimate the average slip rate of the Morne Piton  
145 at about 0.5±2 mm.yr<sup>-1</sup> since 330 Ka. Regarding the uplifted terraces they estimated a  
146 maximum earthquake moment magnitude ( $M_w$ ) ranging from 5.8 up to 6.5 with a 400-  
147 1000 to 1400-3300 years of recurrence time, respectively (250 km<sup>2</sup> of estimated  
148 ruptured area). Moreover, it was later demonstrated that this plateau emerged between  
149 1.77 and 1.07 Ma (magnetostratigraphic Chron 1R2r: Cornée et al., 2012; Münch et al.,  
150 2014; De Min et al., 2015; Léticée et al., 2019; Cornée et al., 2021). Note that considering  
151 an older age for the Plateau emergence would drastically lower the slip rate estimate and  
152 increase the recurrence time calculated by Feuillet et al. (2001).

153 Upper plate seismicity in the Marie-Galante Basin provided by (i) CDSA Seismic  
154 database (Antilles Seismological Data Center - Bengoubou-Valerius et al. (2008); Massin et  
155 al.(2021)), (ii) IRIS database (IRIS <https://www.isc.ac.uk> (Figure 2B) and (iii) the  
156 deployment of Ocean Bottom Seismometers (OBS) (Ruiz et al 2013; Bie et al., 2019)  
157 shows a widely distributed pattern of moderate magnitude earthquakes ( $M_w \leq 5.3$ ), with  
158 the exception of the 2004 seismic cluster in Les Saintes. Wide Angle Seismic (WAS)  
159 profiles together with earthquakes data indicate a seismogenic crustal thickness limited  
160 to the first 15-20 km west of Marie-Galante suggesting a brittle-ductile transition at this  
161 depth (Kopp et al., 2011; Ruiz et al 2013; Gonzalez et al., 2017; Padron et al., 2021).  
162 Among the very few focal mechanisms available in the Marie-Galante Basin (Gonzalez et  
163 al. 2017), the 25 February 2014  $M_w$  3.8 earthquake occurred beneath the southern



164 Grande-Terre platform and shows pure normal motion along sub-E-W trending nodal  
165 planes (Gonzalez et al. 2017, Event n°9, hypocentral location accuracy of ca. 5 km, Figure  
166 2C). The location, depth and nodal plane characteristics (57° dip and N102°E) of the  
167 earthquake indicate that the event may correspond to a rupture along the Gosier fault  
168 system, which is the only major fault system in the vicinity of the hypocentral location  
169 able to trigger such magnitude earthquake. Feuillet (2000) provided more than 20 focal  
170 mechanisms for magnitude  $2 < M_l < 3.7$  and one  $M_s = 5.6$  earthquakes located in and around  
171 the Marie-Galante Graben. All focal mechanisms show nearly pure normal motion along  
172 sub-E-W trending nodal planes, consistent with kinematics indicators observed along the  
173 Gosier and Morne Piton Faults. This tectonic pattern is confirmed by GNSS velocities  
174 which indicate that a small trench-parallel extension is accommodated in the upper plate  
175 forearc (van Rijsingen et al., 2021).

176 Two historical earthquakes are reported along these two fault systems (Feuillet et  
177 al., 2011b): (i) the 16 May 1851 earthquake with a maximum intensity of VII recorded in  
178 the southeastern part of Basse-Terre, is attributed to the Morne Piton Fault with an  
179 estimated magnitude  $M_w = 6.0$  (Feuillet et al., 2011); and (ii) the 29 April 1897 earthquake  
180 with a maximum intensity of VIII recorded in the Pointe-à-Pitre area being either  
181 attributed to the Gosier Fault system with an estimated magnitude  $M_w = 5.5$ , or to the  
182 Montserrat fault zone, with an estimated magnitude  $M_w = 6.5$  (Bernard and Lambert,  
183 1988; Feuillet et al., 2011). Overall, at the latitude of Guadeloupe, regional earthquake  
184 data suggest that normal fault systems are active with an ability of generating  $M_w$  6  
185 earthquakes potentially able to trigger tsunami (as explained, for example, in Roger et al.,  
186 2019).

187 Southwest of the Marie-Galante Basin, the 2004  $M_w$  6.3 earthquake (Bazin et al.,  
188 2010; Feuillet et al., 2011) showed that upper plate crustal faults can generate strong  
189 earthquakes and tsunami. The main shock occurred along the NNW-SSE trending, ca. 40  
190 km-long arc-parallel Les Saintes Fault System (Feuillet et al. 2011; Leclerc et al. 2016).  
191 The recurrence of such a rupture is estimated to be a few hundred years or more (Escartin  
192 et al., 2016; Escartin et al., 2018; Feuillet et al. 2011; Le Friant et al., 2008). Focal  
193 mechanisms of the main shock as well as five aftershocks provided an overall pure  
194 normal motion along NNW-SSE nodal planes (Figure 2D). Source models from Salichon  
195 et al. (2009), Bazin et al. (2010), and Feuillet et al. (2011), well constrained by the long  
196 duration of the aftershock sequence, proposed a main source localized along the N135°E



197 trending, 50°E dipping Roseau Fault (westernmost fault of Les Saintes fault system) with  
198 a 30 km-long and 21 km-downdip width fault plane. Aftershock seismicity reactivated  
199 several nearby conjugate faults with a maximum seismic depth at *ca.* 15 km. The main  
200 rupture occurred at two asperities located 8 km below the surface with a maximum slip  
201 of 1.8 m, and propagated to the surface triggering a coseismic offset of the seafloor of 0.3-  
202 0.6 m along a *ca.* 10 km-long segment. Escartin et al. (2016) investigated the fault scarp  
203 by the mean of HR bathymetry highlighting a 3 km-long, up to 0.9 m-high scarp but  
204 concluded that part of the observed slip may be post-seismic. The Les Saintes earthquake  
205 generated up to 2 m-high tsunami waves and a maximum horizontal run-up of 42 m in  
206 some bays of Les Saintes (Zahibo et al., 2005; Le Friant et al., 2008; Cordrie et al., 2020).  
207 However, tsunami models using fault parameters based on seismological data resulted in  
208 an under estimation of the tsunami wave amplitude and run-up (Le Friant et al., 2008).  
209 Cordrie et al. (2020) consider that their best fit models require greater slip on the fault  
210 plane and a greater magnitude for the earthquake than those given by the seismological  
211 data in order to accurately reproduce the observed tsunami, suggesting that the observed  
212 scarp is the surface expression of co-seismic slip (source parameters:  $M_w=6.4-6.5$  – fault  
213 plane 15x15 km – Strike N325°E – Dip 55°E – rake  $ca.90^\circ$  - slip=2.5-3.5 m).

214 Over the last ~500 years of historical written archives in the Lesser Antilles, a few  
215 dozen confirmed tsunamis from different origins (local, regional or far-field sources  
216 including earthquakes, landslides, volcanic eruptions or combinations of them) have  
217 been reported. Starting with the 16 April 1690  $M_s\sim 8.0$  Barbados earthquake (which  
218 presumably triggered the first reported tsunami in the Lesser Antilles), it includes the  
219 widely studied 1 November 1755 Lisbon transoceanic tsunami (*e.g.*, Gutscher et al., 2006,  
220 Accary and Roger, 2010; Roger et al., 2010, 2011, Martinez-Loriente et al., 2021) and the  
221 18 November 1867 Virgin Islands tsunami (*e.g.*, Zahibo et al., 2003, 2005; Barkan and ten  
222 Brink, 2004).

223 On the basis of an extensive literature review, including cross-checking of  
224 information, we conclude that only four tsunamis reported in Guadeloupe are likely of  
225 upper crustal seismic origin (Mallet, 1853, 1854, 1855; Lander, 1997; Zahibo and  
226 Pelinovsky, 2001; Lander et al., 2003; O'Loughlin and Lander, 2003; Zahibo et al., 2003;  
227 Accary and Roger, 2010; Nikolkina et al., 2010; Roger et al., 2013; online databases:  
228 NGDC/WDS, 2023; TL/ICMMG, 2023). These tsunamis have been observed or recorded  
229 following earthquakes occurring on regional faults (indicated magnitude and epicenter





230 coordinates are from the USGS online earthquakes catalogue): the Mw~8.0-8.5  
231 earthquake on 8 February 1843 (NE of Guadeloupe, 16.73°N, 61.17°W) and the Mw 7.2  
232 earthquake on 25 December 1969 (SE of Guadeloupe, 15.648°N, 59.694°W) are arguably  
233 attributed either to a rupture along the megathrust or to upper plate faulting ; the Mw 6.5  
234 earthquake on 16 March 1985 (along the Harvers-Montserrat-Bouillante fault system  
235 between Montserrat and Nevis, north of Basse-Terre, 17.013°N, 62.448°W); and the Mw  
236 6.3 earthquake on 21 November 2004 (Along the Les Saintes fault system, south of Basse-  
237 Terre, 15.679°N, 61.706°W)(Figure 1). As magnitude of crustal earthquakes is  
238 constrained by fault length, events occurring along such crustal fault show a much smaller  
239 magnitude than megathrust earthquakes but they may form large seafloor offsets. Thus,  
240 most crustal earthquakes able to trigger a tsunami do not produce significant sea surface  
241 deformation (only a few centimeters amplitude in most cases) compared to subduction  
242 interface earthquakes. Associated tsunamis are typically only visible on pressure gauge  
243 records (coastal gauges or DART stations) after processing the data (*e.g.*, de-tiding, high-  
244 frequencies filtering, etc.).

245

### 246 **3. Material and method**

#### 247 *3.1 Seismic lines*

248 We present eight multichannel seismic (MCS) lines acquired during five  
249 oceanographic campaigns (location on Figure 3A). These include high-resolution sparker  
250 source seismic data from KaShallow 1 (Lebrun et al., 2009) and GEOBERYX03  
251 oceanographic campaigns (Thinon and Bitri, 2003;Thinon et al., 2004 and 2010), mid  
252 resolution GI airgun arrays seismic data from KaShallow 2 (Lebrun et al., 2009) and  
253 Aguadomar (Deplus et al., 1999) cruises, and deep penetrating MCS data from the  
254 Sismantilles 1 seismic experiment (Hirn, 2001) (Table 1).

255 Sismantilles 1 seismic data have been processed using CGG-Veritas Geovecteur®  
256 software on board the R/V Nadir (Hirn et al., 2001). Processing includes band pass  
257 filtering, internal and external mute, one step velocity analysis, NMO correction, stack,  
258 predictive deconvolution and post-stack constant water-velocity time migration. The  
259 KaShallow 1 and 2, Aguadomar and Geoberyx have been processed with Seismic Unix  
260 software (Cohen and Stokwell, Center for Wave Phenomena, Colorado School of Mines).  
261 The seismic processing includes band pass filtering, sea waves and spherical divergence  
262 corrections, constant velocity or simple velocity gradient NMO correction and stack, and





263 constant water-velocity time migration. The reflection seismic lines are in milisecond  
264 two-way-travel-time (mstwtt). The velocities of the Wide Angle Seismic refraction (WAS)  
265 profiles are in second two-way-travel-time (stwtt).

266

### 267 *3.2 Bathymetry*

268 High-resolution bathymetric data were acquired during the KaShallow2  
269 oceanographic campaign (Lebrun, 2009) using the Simrad EM300 multibeam  
270 echosounder. We merged this data with Aguadomar (Deplus, 1999) and Sismantilles 2  
271 (Laigle et al., 2007) cruises Simrad EM12 Dual multibeam echosounder data available for  
272 the Marie-Galante Basin. Vertical accuracy for these echosounders is plurimetric for  
273 typical water depth found in the Marie-Galante Basin (<2000 m below sea-level, noted  
274 bsl hereafter). Near-shore (0-200 m bsl) and onshore, very high-resolution bathymetric  
275 and topographic data comes from the Litto3D database -  
276 (<https://www.geoportail.gouv.fr/donnees/litto3d> last accessed on September 2020-  
277 that includes airborne lidar survey and Kashallow-3 multibeam data acquired with a  
278 RESON Seabat 8101 multibeam echosounder. The vertical accuracy for this second  
279 dataset is better than one meter. We used software to process the data and to produce a  
280 25 m grid spacing Digital Elevation Model of the Marie-Galante Basin and surrounding  
281 islands. Maps are produced using the open-access QGIS software (<https://www.qgis.org>)

282

### 283 *3.3 Depth and time calibration of main geological boundaries.*

284 In order to measure offsets of unconformities on time-migrated seismic lines we  
285 need to constrain the seismic velocities within the sediments. We used velocities from the  
286 WAS profile (Kopp et al 2011) in the south of Marie-Galante, that trends parallel to the  
287 MCS line Agua116 (Cornée et al., 2023). The WAS velocities in the *ca.* 0.4 stwtt thick upper  
288 unit (MG-MS3 – Cornée et al., 2023) ranges between 2 and 2.5 km/s. The 3.25 km/s  
289 isochrones mimic the base of unit MG-MS2 and the 4.5 km/s isochrones follow the  
290 acoustic basement below MG-MS1. Moreover, Kashallow 2 cruise MCS data (Table 1)  
291 acquired with a 600 m long streamer allows us to determine the Normal Move Out  
292 velocities down to a depth of *ca.* 0.75 stwtt in well-layered units such as shown on the  
293 seismic lines (Figure 3). Once converted into interval velocities using the “Hewitt Dix  
294 formula”, we determine velocities in the upper unit from 1500 to 2750 m/s (Dix, 1995).  
295 Therefore, we use 1500 m/s in the water and 2000 m/s and 2500 m/s in the sediments



296 to estimate (and bound) the depth of unconformities observed on time-migrated seismic  
297 lines (Table 2).

298 Offshore, several first order unconformities and sedimentary units were  
299 accurately dated using bio-stratigraphy analysis or radiochronology (Bouysse and  
300 Mascle, 1994; KaShallow Reasearch Program results: Cornée et al., 2023; De Min, 2014;  
301 De Min et al., 2015; Münch et al., 2013). The deepest dated unconformity, MG-SB2, which  
302 corresponds to the top of the MG-MS1 sequence, occurs on seismic lines east of Marie-  
303 Galante (thick orange line on Figure 5, lines AGUA97 – K09-09 – K09\_45 - Sis7C). Along  
304 the seismic line Agua 97, the F8 fault scarp has been sampled at 514 m bsl just beneath  
305 the unconformity (KaShallow Cruise ROV dive, Figure 6). The samples, BMG2 and 4,  
306 yielded a Late Burdigalian/earliest Langhian age (Cornée et al., 2023). Thus, we propose  
307  $16 \text{ Ma} \pm 1 \text{ Ma}$  for the age of MG-SB2. Above, another regional unconformity MG-SB3  
308 (Cornée et al., 2023) is identified east of Marie-Galante. It corresponds to the top of MG-  
309 MS2 sequence (thick purple line on the Figure 5 lines Agua97 – K09-09-08 – K09-45-44  
310 – Sis7C). The age for this surface is bracketed between the overlaying Late Messinian GT  
311 carbonate platform (zones N18,  $5.8\text{-}5.33 \text{ Ma}$  –Cornée et al., 2023) and the underlying  
312 sedimentary unit dated Late Tortonian  $8.57 \pm 0.43 \text{ Ma}$  (Ar-Ar, Münch et al., 2014). We  
313 thus consider  $7 \pm 1.5 \text{ Ma}$  for the age of MG-SB3. West of Marie-Galante, the angular  
314 unconformity on line K09-90 North-West of Marie-Galante may corresponds to MG-SB3  
315 (Figure 4). However, this reflector is too deep to be followed across the fault system.  
316 Within the uppermost sequence, MG-MS3, a remarkable unit boundary corresponding to  
317 a second order unconformity, can be easily correlated throughout the basin and onshore  
318 (red thick line on Figure 4). This unit boundary is Middle-Late Piazencian offshore and  
319 correlates onshore with the 3–2.9 Ma tectonically-induced erosional unconformity SB1  
320 (see above; Cornée et al., 2023). Along the seismic line Ber03-30-31, the fault scarp  
321 immediately north of F3 and F4 has been sampled at 283 m bsl (KaShallow Cruise ROV  
322 dive, Figure 4). Samples, BC1 and BC2, yielded ages of  $1.33 \pm 0.23 \text{ Ma}$  and  $1.15 \pm 0.12 \text{ Ma}$ ,  
323 respectively (Ar<sup>40</sup>/Ar<sup>39</sup> ages on plagioclases, Münch et al., 2013; 2014). These samples  
324 correspond to a prominent seismic reflector within the upper unit of MG-MS3 sequence  
325 that can also be easily correlated through all the seismic lines west of Marie-Galante. We  
326 thus retain an average age of  $1.29 \pm 0.26 \text{ Ma}$  for this seismic reflector (green line on Figure  
327 4).

328



### 329 *3.4 Tsunami modeling*

330 In order to test the tsunamigenic potential of the different proposed faults herein,  
331 several rupture scenarios have been elaborated and are presented hereafter.

332 Numerical simulations of tsunami generation and propagation were carried out  
333 using COMCOT software (Cornell Multi-grid Coupled Tsunami: Liu et al., 1998; Wang,  
334 2008; Wang and Power, 2011). COMCOT is widely used by the research community and  
335 constantly tested notably through various real tsunami cases (e.g. Prasetya et al., 2011;  
336 Gusman et al., 2019; Paris et al., 2021; Gusman et al., 2022; Roger et al., 2023). COMCOT  
337 uses a modified staggered finite-difference scheme to solve linear and non-linear shallow  
338 water equations in either spherical or Cartesian coordinate systems throughout a set of  
339 nested grids allowing refinement of the bathymetric resolution in coastal areas. A two-  
340 way nested grid configuration is implemented in the model to balance computational  
341 efficiency and numerical accuracy (Wang 2008; Wang and Power 2011).

342 For this study, nesting has been used with two grid levels: the first grid is a 0.5  
343 arcmin (~900 m) resolution grid of the Lesser Antilles (extent: 295°E, 302°E, 12°S, 18°S)  
344 built from the global dataset GEBCO 2021 (GEBCO Compilation Group, 2021); the second  
345 grid is a 3.75 arcsec (~115 m) spatial resolution grid focusing on the Guadeloupe  
346 Archipelago and Dominica Island, including the investigated faults location as shown on  
347 Figure 1 (extent: 297.92°E, 300.22°E, 14.94°N, 16.717°N). This second grid has been built  
348 from different datasets including the aforementioned bathymetric data (§ 3.2). The  
349 highest resolution and the more recent data have been kept first. Data gaps have been  
350 filled in with GEBCO 2021 (GEBCO Compilation Group, 2021) for offshore regions, and  
351 SRTM version 3.0 Global 1 arc second data (NASA SRTM, 2013) for onshore regions.  
352 Continuity of the different datasets has been ensured using kriging interpolation, which  
353 has proven to be one of the best methods to apply in order to produce a well-defined DEM,  
354 especially for smooth transitions between different resolution areas (e.g. Bernardes et al.,  
355 2006; Arun, 2013; Ajvazi and Czimber, 2019). Note that Dominica was included in the  
356 second grid was to look at potential effects which could occur between the different  
357 islands and also assess the potential tsunami threat resulting from the Morne Piton  
358 scenario on this neighboring island.

359 The initial displacement of every simulation is calculated by COMCOT considering  
360 an instantaneous rupture of the fault using Okada (1985)'s rupture model, and  
361 transmission of the deformation to the water column above is considered instantaneous.



362 Calculations of wave propagation have been done at mean sea level (MSL) assuming a  
363 constant Manning's roughness coefficient of 0.011 for the seabed friction (Wang et al.,  
364 2017). A higher friction coefficient leads to more energy dissipation of tsunami waves,  
365 especially in shallow waters, slowing down their speed and reducing their amplitude and  
366 impact (e.g. Dao and Tkalich, 2007). Considering the limited extent of the interest zone  
367 (~250km x 200km), the rupture parameters (leading to a small coseismic rupture) and  
368 the objective to look at potential localized effect as inter-islands resonance, tsunami  
369 waves propagation time was set to 10 hours.

370

#### 371 **4. RESULTS**

372

##### 373 *4.1 The Morne Piton Fault system*

374 The HR bathymetric data presented here above (section 3.2) allows to refine the  
375 structural pattern of the Morne Piton Fault system, especially offshore (Figures 3A - B).  
376 The fault system splays eastward from the N120-N135°E trending Eastern Les Saintes  
377 fault system located east-south-east of Basse-Terre to the N110-115°E trending Petite-  
378 Terre fault system south-south-east of Grande-Terre (Figures 2 and 3). Thus, the fault  
379 zone spreads over a 5-8 km wide and 50 km long zone with an average N100°E trend.

380 The main fault scarp of the Morne Piton fault system is the southernmost one,  
381 along which 9 fault segments of 1-10 km length can be identified (Figure 3B). From west  
382 to east, the F1 segment trends N110° and then the fault steps left along the N75°E  
383 trending F2 segment. A little farther east, the fault cuts the northern Colombie Bank and  
384 the eastern Marie-Galante platform along closely spaced N90E trending left or right  
385 stepping segments F3, F3', F4 and F5. Across the island, the F6 segment is a N130°N  
386 trending, 6 km long right step relay linking the F5 segment to the F7 N90°E trending one.  
387 Further east offshore Marie-Galante, two N80°E trending fault segments, F8 and F9,  
388 arrange as overlap right steps. There, the fault scarp vanishes in just a few kilometers. To  
389 the east of the line Sis7C, neither the sediments nor the basement are affected by the  
390 north-dipping Morne Piton Fault system (Figure 5). In contrast, the seismic line Sis7C  
391 shows that the basement is southwardly downthrown by the Petite-Terre fault system,  
392 along south dipping active and sealed faults to the north and south of the Morne Piton  
393 Fault system, respectively (Figure 5 location on Figure 3A) . West of Marie-Galante, the  
394 Morne Piton Fault system widens as closely spaced fault splays trending N95°E to N100°E



395 link the main fault scarp (F2, F3 and F4) to the antithetic Goyave Fault system or die  
396 westward (Figure 4 location on Figure 3A). Eastward of the F6 segment, some synthetic  
397 and a few antithetic faults splay northeastward and link with the N110-115°E Petite-  
398 Terre Fault system.

399         The mean fault-scarp height west of Marie-Galante Island is ca. 100 m (Figure 3C).  
400 Across Marie-Galante Island, the mean fault-scarp height reaches 200 m and controls the  
401 staircase morphology of the island. East of the island, the Marie-Galante Canyon carved  
402 the sedimentary units, clearing some of the fault planes increasing their apparent scarps  
403 heights up to 400 m. To the east, the canyon meanders and cuts through the eastern tip  
404 of the Morne Piton Fault system (Figure 3 B and C). West of the island, at the vicinity of  
405 the volcanic island of Basse Terre, either recent deposits or the uppermost sedimentary  
406 units seal most of the faults. These observations seem to indicate that the sedimentary  
407 rate west of Marie-Galante and the erosional rate east of Marie-Galante (in the canyon)  
408 exceed the vertical slip rate of the fault.

#### 409 *4.2 Vertical slip rate estimates along the Morne Piton Fault system*

410         To assess the average vertical slip rate along the Morne Piton Fault system, we  
411 estimated the fault offset of key dated reflectors across the entire length of the fault  
412 system (Figures 4 and 5 – Table 2). West of Marie-Galante, the main offset of the  $1.29 \pm$   
413  $0.26$  Ma seismic reflector (green on Figure 4) increases from west to east (i.e., from the  
414 westernmost extremity of the fault toward its center). Close to the eastern shore of Basse-  
415 Terre Island (Figure 4, profile K09-96, and Table 1), the 1.29 Ma reflector is downthrown  
416 by 110-115 m. Eastward, the reflector offset increases up to 230-257 m (Figure 4, line  
417 K09-90, K08\_24 and Table 2) and reaches a maximum of 300-322 m (Figure 4, lines  
418 ber03\_30-31, K08-59). Accordingly, the number of sealed structures across the fault  
419 system decreases eastward (Figures 3 and 4). Thus, West of Marie-Galante, the Morne  
420 Piton Fault system accommodates a vertical slip rate increasing eastward up to  $0.25 \pm$   
421  $0.08$  mm.yr<sup>-1</sup> over the last  $1.29 \pm 0.26$  Ma (Table 2). The  $2.95 \pm 0.05$  Ma Unit Boundary  
422 (red line on figure 4) can only be correlated across the fault system along the K08-59  
423 seismic line. Growth strata are observed in the deposits above the 2.95 Ma unit boundary  
424 (Figure 4, gray shadow on seismic lines), attesting for syn-sedimentary fault activity. This  
425 unit boundary offset reaches 550-620 m, leading to  $0.20 \pm 0.02$  mm.yr<sup>-1</sup> average vertical  
426 slip rate over the last  $2.95 \pm 0.05$  Ma. These two estimates are compatible within their



427 uncertainties and suggest a steady slip rate of the Morne Piton Fault since *ca.* 3 Ma at  
428 least.

429 East of Marie-Galante, the MG-SB2 sequence boundary dated to  $16 \pm 1$  Ma (orange  
430 in Figure 5) is the only reflector that can be correlated on both sides of the fault system.  
431 In the hanging wall of the fault, the younger MG-SB3  $7 \pm 1.5$  Ma boundary (Purple in Figure  
432 5) as well as a large part of the fault scarp are eroded by the Marie-Galante Canyon. The  
433 seismic line K09-09 (Figure 5) shows that the MG-SB3 unconformity records the Morne  
434 Piton Fault inception: in the footwall of the fault, the stratigraphy of MG-MS2 sequence  
435 (comprised between MG-SB2 and MG-SB3) shows conformal deposits flexed upward  
436 while approaching the fault, whereas MG-MS3 deposits onlap onto MG-SB3 and present  
437 clear growth strata. We thus propose that the  $16 \pm 1$  Ma sequence boundary is pre-  
438 tectonic and is titled by the fault since its inception  $7 \pm 1.5$  Ma ago (the age of MG-SB3;  
439 Figure 5, profile K09-45-45). Along the fault system East of Marie-Galante we calculated  
440 the strain rate from MG-SB2 offset since  $7 \pm 1$  Ma. From east to west the slip rate ranges  
441 from  $0,067 \pm 0,03$  mm.yr<sup>-1</sup> at the K09\_44-45 seismic line, to  $0,071 \pm 0,02$  mm.yr<sup>-1</sup> along the  
442 K09\_08-09 line. Seismic line Agua97 (Figure 5) presents the greatest offset of MG-SB2.  
443 However, this seismic line does not cross the southernmost F7 segment (the water depth  
444 is too shallow for ship navigation in the footwall compartment). We estimated the depth  
445 of MG-SB2 in the footwall compartment from the closest seismic line available that  
446 crosses the fault located 1 km east of the Agua97 line. We obtain an offset of 977-995 m  
447 leading to a maximum vertical slip rate of  $0.15 \pm 0.05$  mm.yr<sup>-1</sup> since  $7 \pm 1.5$  Ma (Table 2).  
448 Consequently, we propose that i) the vertical slip rate accommodated by the Morne Piton  
449 Fault system increases progressively from each extremity of the fault toward its center,  
450 and ii) that the Morne Piton Fault system is characterized by a constant slip rate of  $0.20$   
451  $\pm 0.05$  mm.yr<sup>-1</sup> since its inception, *i.e.* 7 Ma ago.

#### 452 4.3 Earthquakes parameters of Tsunami modeling

453 ROV dive along the ber03\_30-32 seismic line allowed observation of one of the  
454 main morphologic scarps of the Morne Piton Fault system across the F2 and F3' segments  
455 (Figures 3 and 6). Across the upper plateau, between F2 and F3', we observed several  
456 N90°E trending fractures parallel to the fault segments (Figure 6A). While descending  
457 across the F3' scarp, the slope progressively steepens up from 45° at 157 m bsl to more  
458 than 80° at 280 m bsl just a few meters above the toe of the scarp (Figure 6A, B and C).



459 This morphology suggests a ca. 128 m-high cumulative scarp for the F3' segment at that  
460 location. The very last meter of the fault scarp above the toe of the slope presents a 100  
461 cm high polished vertical surface, partly altered, showing dip-slip striations indicating  
462 pure normal motion along this fault segment (Figure 5D E and F). This exposed and partly  
463 altered fault slip plane breaches the sea floor at high angle. Such a polished striated fault  
464 scarp morphology is similar, although more altered, to the co-seismic fault scarp  
465 observed at the toe of the Roseau Fault plane, after the Les Saintes earthquake (Escartin  
466 et al., 2016). We conclude that this observation of the Morne Piton polished striated scarp  
467 may correspond to one of the last co-seismic scarps formed during a major earthquake  
468 (including possible post-co-seismic slip motion) along this fault. Alteration of the fault  
469 slip plane suggests that the slip event occurred tens to several hundred years ago, *i.e.*, this  
470 fault slip plane may correspond to a pre-instrumental earthquake (see discussion). From  
471 this observed scarp we obtained a ratio of last event scarp over total scarp height (proxy  
472 for the cumulative slip as determined on Figure 3) of ~2,6%. With this ratio we calculated  
473 an average scarp of ~75 cm along the whole length of the fault and a maximum scarp of  
474 2 m. Such an average scarp value corresponds to the surface expression of a magnitude  
475  $M_w \sim 6.5$  earthquake using the criteria of Wells and Coppersmith (1996), Leonard (2010)  
476 or Thingbaijam et al. (2017). The same studies also provide a calculated maximum  
477 displacement of ~2m, consistent with the maximum observation along the scarp.  
478 Moreover, the 45 km total length of the Morne Piton Fault system measured from HR  
479 bathymetry, together with the width of the fault given by the 10 to 15 km thick  
480 seismogenic crust, lead to a rupture area ranging between ~ 450 to 675 km<sup>2</sup> that would  
481 generate a magnitude  $M_w \sim 6.5 \pm 0.5$  earthquake corroborating the afore range of  
482 magnitude deduced with other observations (e.g., Wells and Coppersmith, 1996;  
483 Leonard, 2010; Thingbaijam et al., 2017). Hereafter, we use these parameters to evaluate  
484 the potential tsunami hazard from the Morne Piton Fault for a worst-case plausible  
485 scenario.

486

#### 487 *4.4 Related tsunami hazard*

488 We present a worst-case plausible scenario, related to a rupture along all the  
489 identified segments of the Morne Piton Fault as these 1 to 10 km-long segments most  
490 probably root in-depth along a single fault zone (Feuillet et al., 2004). We rule out the  
491 eventuality of testing a single 10 km-long segment of the Morne Piton Fault system





492 rupture as it would generate a  $M_w < 6.0$  earthquake and would thus unlikely consist in a  
493 tsunami source (Roger et al., 2019). Here, we use a maximum plausible scenario that  
494 would generate a tsunami with a significant energy/amplitude to accurately highlight the  
495 potential consequences of tsunami waves' propagation and interaction with the peculiar  
496 shallow reliefs and major embayment located in and around the Marie-Galante Basin.  
497 Quantifying horizontal run-up at the coast and assessing tsunami risk following rupture  
498 along this fault is out of the scope of the present study as such quantifications necessitate  
499 a better knowledge of the fault dynamic itself (return period of large events, etc.).

500 The rupture parameters for the different identified segments of the fault shown on  
501 figure 3B are provided in Table 3. Geographic location of the center of the fault plane and  
502 azimuth are provided based on our structural analysis (section 4.1 and 4.3). Neither  
503 seismic lines which illustrate only a few hundred of meters nor in-depth earthquake  
504 distributions (which is not enough resolved) allow to estimate the dip of the Morne Piton  
505 Fault system. Thus, after showing that the influence of dip on surface deformation is  
506 neglectable we choose a mean dip of  $75^\circ$  for the fault segments after Feuillet et al. (2004).  
507 The shape of the rupture area (along-strike length x downdip width) and a slip of 1.89 m  
508 is implemented for each segment in order to fit with a total fault surface of ca.  $500 \text{ km}^2$ ,  
509 corresponding to a magnitude  $M_w 6.5$  earthquake. Finally, conformably to pure dip slip  
510 striations observed along the F3' segment (section 4.3) and the F7 segment (Feuillet et al.  
511 2002), we apply a rake of  $90^\circ$  (pure normal faulting mechanism as observed by Feuillet  
512 et al., 2004 at Anse Piton and by the ROV picture of the present study). Fault segments F8  
513 and F9 are not straight, for the purpose of modeling they have been divided into F8-F8'  
514 and F9-F9'.

515 The initial surface elevation directly resulting from the Okada (1985) formulation  
516 is indicated in Figure 7. Due to the high inclination of the fault planes (dip =  $75^\circ$ ) dipping  
517 globally southward, a profile cut of the initial displacement is represented from the north  
518 to the south by a crest (positive elevation) and a trough (negative elevation). At  $t=0$ , the  
519 shallow water equations take over from this initial deformation and the propagation of  
520 the tsunami waves is calculated over the nested grids at adequate time steps. Figure 8  
521 presents the state of the virtual water surface at six different times of the tsunami waves  
522 propagation from 1 to 16 minutes. The wave front initially parallel to the fault axes ( $t \leq 1$   
523 min) is progressively influenced by the bathymetry within the very first minutes  
524 following the rupture, leading to an anisotropic propagation of the waves showing



525 variability in space and time. In addition, the fact that the fault literally crosses Marie-  
526 Galante leads to the tsunami source being divided in two independent sources located on  
527 the west and east of this island: two tsunamis are therefore generated and called TsuW  
528 (on the west) and TsuE (on the east) hereafter. These two tsunamis propagate from their  
529 origin and wrap around Marie-Galante as shown at  $t=4$  min of propagation. Then,  
530 between 4 and 9 min, the two tsunami fronts meet on the north and south of Marie-  
531 Galante. Meanwhile, the propagation of the TsuW waves meet the shallow waters of the  
532 Banc Colombie shoal (approx. coordinates:  $15.98^{\circ}\text{N}/-61.43^{\circ}\text{W}$ ; minimum water depth of  
533 less than 50m), west of Marie-Galante: the waves' amplitude increases and their  
534 interaction leads to a constructive interference resulting in a "new" tsunami source at the  
535 Banc Colombie shoal, mainly showing a negative wave propagating southward with some  
536 extensions toward Marie-Galante on the east and Les Saintes on the west. This relatively  
537 high amplitude negative wave is shown by VG\_1 on figure 10 with a peak to trough value  
538 of  $\sim 0.6$  m. VG\_2 and VG\_3 also show it to a lesser extent a bit later.

539 Approaching the coasts, wave shoaling takes over, the reduction in water depth  
540 slowing down the waves and simultaneously increasing their amplitude. It leads to wave  
541 amplification as particularly shown along Marie-Galante north shore, the southeast coast  
542 of Basse-Terre and the south of Petite-Terre.

543 After 10 hours of tsunami propagation, the maximum values of wave amplitude  
544 reached on each point of the simulation domain are shown in Figure 9. The overall impact  
545 of such an event is that the maximum wave amplitude is not going over 1.2 m, carefully  
546 considering the 100 m resolution of the simulation domain: in fact, a higher resolution  
547 grid would probably show higher wave amplitude in very localized areas because of  
548 interaction with small underwater structures not represented at this resolution and non-  
549 linear effects. The patterns of those amplitudes indicate that not only the fault region but  
550 also some coastal regions are exposed to tsunami waves of 50 cm or more. It is the case  
551 for the neighboring coasts of Marie-Galante, southeast Basse-Terre, south Grande-Terre  
552 and the natural reserve of Petite-Terre. The southeast coast of Basse-Terre is particularly  
553 exposed with waves of more than 1 m (Figure 9a). A focus on Les Saintes Archipelago  
554 highlights also wave amplitudes of more than 1 m, even between the islands (Figure 9b).  
555 The northeast coast of Dominica is also affected but to a lesser extent (maximum wave  
556 amplitudes of  $\sim 50$  cm). Further high-resolution simulation would help to correctly assess  
557 the related hazard on this island. Virtual sea-level gauges have been added at different



558 locations of grid 2 (Figure 9) in order to check if the model is stable and to look for  
559 possible resonance (especially in Les Saintes Archipelago). The raw signal of seven VG  
560 (top figure 10) highlights a clear decrease of the amplitude over the time on all stations.  
561 However, for stations VG\_1, VG\_2 and VG\_3, a low-frequency oscillation is clearly visible  
562 and lasts for at least 10 hours. The amplitude spectrums on these three stations show that  
563 two peaks with a period of ~6.5 min and 17 min respectively are present on the three  
564 signals at Les Saintes, which is not the case for the stations out of the archipelago.

565

## 566 **5. Discussion**

### 567 **5.1. Implications a local and regional scales**

568 The highest magnitude earthquakes and strongest tsunami produced at  
569 subduction zones are expected to originate from rupture at the plate interface  
570 megathrust. However, historical records in the Lesser Antilles reveal that neither the  
571 1843 Mw 7.5-8.5 nor the 1839 Mw 7.5-8.5 largest known earthquakes, although  
572 destructive, have been followed by large tsunamis. However, Roger et al. (2013) showed  
573 that the simulation of a Mw 8.5 1843-like megathrust earthquake would have produced  
574 wave amplitudes of 5 m and more along the exposed coasts of Guadeloupe, which was not  
575 reported in coeval documents. Feuillet et al. (2011) explain these two major earthquakes  
576 by the great depth of the rupture along the megathrust that lead to little seafloor  
577 deformation. However, numerical simulation of worst-case scenarios for these two  
578 ruptures along the megathrust evidence the possibilities of tsunami amplitudes up to 10  
579 meters and above in some embayment (Roger et al., 2013; Colon-Useche et al., 2023).

580 Les Saintes earthquake demonstrated that upper plate normal faults may generate  
581 Mw>6 tsunamigenic earthquakes in the Lesser Antilles. Les Saintes tsunami produced up  
582 to 2 m high waves at the coast and 42 m distance run-up in a peculiar embayment  
583 (Cordrie et al. 2020). Such normal faults are prone to be tsunamigenic because their  
584 rupture is relatively shallow (compared to the megathrust), and their slip motion is  
585 favorable to large seafloor displacement. Together with their proximity to the islands,  
586 they are able to produce metric-high tsunami waves at the coast and tens of meters of run  
587 up distances. Therefore, upper plate crustal faults may represent a major potential  
588 tsunami hazard in the Lesser Antilles islands and particularly in the Guadeloupe  
589 Archipelago as pointed out by the Intergovernmental Oceanographic Commission held in  
590 Fort-de-France in 2019 (IOC-UNESCO, 2020). Similarly to Les Saintes Fault, we assume



591 that the 50 km long Morne Piton Fault poses a potential earthquake and tsunami hazard.  
592 The large scarp we observed at the toe of the Morne Piton Fault suggests recent  
593 tsunamigenic rupture(s) along this structure. However, this scarp might not be related to  
594 the 1851 historical event as the estimated magnitude  $M_w$  5-5.5 for this earthquake  
595 appears too low to explain the observed scarp. Thus rupture of the fault along its whole  
596 length must not be excluded. Several other prominent onshore-offshore faults affect the  
597 seafloor and the topography of the archipelago and may represent both an earthquake  
598 and a tsunami hazard. However, the relationships between faults, earthquakes and  
599 tsunami is not clearly established as shown in the following examples.

600 Along the arc, the Harvers-Montserrat-Bouillante and Les Saintes fault systems are  
601 the most prominent tectonic features (Feuillet et al., 2010). To the south, Les Saintes Fault  
602 system dips east and defines a half-graben (Leclerc et al., 2016). The westernmost fault,  
603 the Roseau fault, ruptured during the 2004  $M_w$  6.3 earthquake and is most probably now  
604 reloading and thus quiet. Recurrence time for this earthquake has been estimated to be  
605 more than 1000 years given the regional slow strain rate. However, the eastern normal  
606 faults of the system offset the seafloor over more than 30 km and present tilted blocks  
607 filled by fan shaped late Pleistocene deposits attesting for recent deformation. In the light  
608 of these observations, the eventuality of a tsunamigenic earthquake along these faults  
609 should be considered. To the North-West along the Harvers segment, a tsunamigenic  
610 rupture occurred in 1985 with strike-slip kinematics and a  $M_w$  6.5 earthquake. Beck et  
611 al., (2012) estimated a recurrence time of 6500-7000 years for such a  $M_w$  6.5 event based  
612 on offset of coseismic deposits in hemipelagites imaged by very high-resolution seismic  
613 lines across the fault. In between these two segments, the Montserrat-Bouillante segment  
614 is seismically quiet except if the 1897 (estimated  $M_w$  7) earthquake occurred along this  
615 fault (Feuillet et al., 2011b). However, no tsunami related to such a rupture has been  
616 reported. Seismic lines across the Montserrat-Bouillante fault (Feuillet et al., 2010;  
617 Legendre, 2018) reveal that the fault offsets the most recent units including the oldest  
618 reflector drilled during the IODP1395, that dates upper Gelasian *ca.* 1.8-2Ma (Le Friant et  
619 al. 2013). Given an offset of 0.3mstwt and a 2000-2500 m/s sediments velocity this  
620 provides a 0.15-0.2  $\text{mm.yr}^{-1}$  slip rate. Thus, the Montserrat-Bouillante segment should  
621 also be considered tsunamigenic.

622 South of Grande Terre of Guadeloupe, the  $N90^\circ E$  trending Gosier Fault system  
623 bounds 45 km of coastal area (Figure 2). The fault system offset the Mid-Pleistocene



624 Grande-Terre plateau that culminates at +150 m from the offshore plateau that rests 15-  
625 20 mbsl (Münch et al., 2013). This suggests a long-term vertical slip rate ca. 0.10 mm.yr<sup>-1</sup>.  
626 To the east of Grande-Terre, the fault crosscuts the MIS5e terrace attesting for Late  
627 Pleistocene activity of the fault. However, evaluation of paleo-seismicity along one  
628 eastern segment of the fault system by the means of trenches allowed the identification  
629 of recent surface ruptures, although superficial deposits remain undated (Terrier and  
630 Combes, 2002).

631 East of Guadeloupe, offshore, the Marie-Galante Basin is bounded to the east by  
632 the Karukera spur, a 75 km long N-S trending submerged plateau that culminates 30 mbsl  
633 to the north offshore La Désirade Island, and gently dips southward down to ca. 1500  
634 mbsl (De Min et al., 2015). The spur is bounded to the west by N150°E to N0°E trending,  
635 west dipping, and normal faults. These faults offset the middle Miocene sequence  
636 boundary (SB2) by up to ca. 2700-2900 m, leading to a long-term vertical slip rate of 0.16-  
637 0.18 mm.yr<sup>-1</sup>. Recent deposits are clearly affected by tectonic activity (Siebert et al.,  
638 2020). Located far from the islands, the earthquake intensity felt onshore would be  
639 relatively low in the island, but a tsunami could propagate across the Marie-Galante Basin  
640 directly toward the arc islands coast.

641

## 642 ***5.2. Slip rate reassessment along the Morne Piton Fault system***

643 Over the last 330 Ka, Feuillet et al. (2004) estimate a bulk slip rate along the Morne  
644 Piton Fault as high as 1 mm.yr<sup>-1</sup> over 330 – 125 Ka then decreasing to 0.3 mm.yr<sup>-1</sup> since  
645 the last 125 Ka. This latter value is close to the long-term slip rate obtained offshore in  
646 this study (Figure 11). These results suggest that the fault may present a fast slip rate  
647 during short periods of time (few 100 ka.) separated by long periods (million years) of  
648 low slip rate. The 1 mm.yr<sup>-1</sup> rate was obtained considering that the terrace T2MG is offset  
649 by the fault by 159 m and dates MIS7e (249 Ka) and the upper-plateau of Marie-Galante  
650 corresponds to an abrasion surface from the MIS9e high stand (330 Ka) (Feuillet et al.,  
651 2004). In La Désirade, the Upper Plateau culminates at 276 m asl (above sea level),  
652 whereas the 330 Ka terrace is at 35 m asl (Lardeaux et al., 2014; Leticée et al., 2019).  
653 Consequently, the hypothesis stating that the plateau emerged 330 Ka ago is ruled out in  
654 Marie-Galante as the youngest formation of Marie-Galante Plateau is not younger than  
655 1.07 Ma (Cornée et al., 2012; Münch et al., 2014). From the geological map of Bouysse et  
656 al. (1993), this later unit rims Marie-Galante Island. Considering this formation as the



657 latest deposit at the Marie-Galante Plateau, it provides a vertical slip rate of 0.15-0.22  
658 mm.yr<sup>-1</sup>, a value close to the 0.2 mm.yr<sup>-1</sup> obtain offshore for the slip rate along the Morne  
659 Piton Fault system (Figure 11). As a consequence, it is not possible to conclude that the  
660 Morne Piton Fault system has short periods of fast slip rate, but it instead probably  
661 evolves through time with a rather constant slip rate of 0.2mm.yr<sup>-1</sup>. This slip rate is five  
662 times slower than previous estimates along Morne Piton, considerably increasing the  
663 earthquake time recurrence along this fault system and thus the time recurrence of  
664 potential associated tsunami.

665         Constraining the fault slip rate at the time scale of one or few seismic cycles may  
666 allow better estimates of seismic and tsunamigenic hazards of the Morne Piton Fault  
667 system. This would require a better knowledge of in-depth fault geometry and  
668 identification of its active segments that could be obtained by the means of a microseismic  
669 survey (using Ocean Bottom Seismometers acquisition over 1-2 years or more). At  
670 present-day, BOTDR laser reflectometry is used to perform long-term monitoring of the  
671 Morne Piton Fault using the network of submarine telecom fiber optic cables connecting  
672 Marie-Galante to the larger islands of Basse-Terre and Grande-Terre (Gutscher et al.,  
673 2023). It is to note that given the slow strain rate and in the absence of rupture occurring  
674 along the fault during the survey period, identifying slip rate across this fault system may  
675 require one to few tens of years. Moreover, very high-resolution seismic data across the  
676 fault in areas of high sedimentation rates (*i.e.*, along the eastern coast of Basse Terre  
677 Island) may constrain the Holocene fault activity. Slip rate estimates will be obtained by  
678 coring and dating of the most recent deformed sediments. Finally, such regional  
679 monitoring will also contribute to a survey of past and potential landslides that may also  
680 be induced by earthquakes and which may locally generate destructive waves.

681

### 682 **5.3. Tsunami simulation**

683         The aim of the tsunami simulation associated to the present study is not to  
684 produce a precise hazard assessment for the islands of Guadeloupe, but rather to give an  
685 overview of what could happen in terms of tsunami generation if the whole identified  
686 Morne Piton Fault segments ruptured together, and to identify a few gaps in terms of  
687 scientific knowledge and operational activities. An accurate hazard assessment study  
688 would require many rupture scenarii including combinations of the segments used in this  
689 study, with variations of their parameters and sensibility tests.



690           The main outcome of the simulation presented hereinabove lies in the fact that  
691 submarine features play an important role on the tsunami waves behavior and amplitude.  
692 Submarine canyons (known to focus the waves: Nazarè Portugal: Martins et al., 2010; do  
693 Carmo et al., 2022; Delpy et al., 2021) and shallow water plateaus located around the  
694 islands slow down the waves which leads to particular propagation patterns like the  
695 wrapping around islands (Figure 8). In fact, it underlines the wrapping effect of the waves  
696 around Marie-Galante associated with two distinct tsunami sources, i.e a primary source  
697 at fault and a secondary one at the Colombie Bank. Such a behavior, already shown in  
698 other regions, is able to considerably amplify the impact of the tsunami on the coast  
699 opposite to the fault rupture (Chadha et al., 2005; Chen et al., 2010). It is important to  
700 notice that the low resolution of the grid used for the present simulations is a limiting  
701 factor in quantifying correctly the wave amplitude along the shoreline. A higher  
702 resolution simulation grid would better reproduce the bathymetric features, especially in  
703 shallow waters, having a non-negligible impact on the waves' behavior and amplitude.

704           The simulation also highlights interesting phenomena that would require further  
705 consideration in the framework of further tsunami hazard studies: wave oscillation,  
706 which could be attributed to a resonance effect, is clearly visible within the Les Saintes  
707 Archipelago, and potential wave trapping is also visible around those islands. If the  
708 second case is purely observation, the resonance between Les Saintes islands is clearly  
709 revealed by the single-sided Fourier amplitude spectrum (Figure 10) and the peak at ~17  
710 min seems to be associated with the negative wave coming time after the initial wave  
711 front and related to the tsunami interaction with the Colombie Bank shoal. The records  
712 provided by the virtual gauges located beforehand within the archipelago (VG\_1, VG\_2 &  
713 VG\_3) clearly shows a long-period oscillation of the signal which is not present on the  
714 gauges located outside of Les Saintes (VG\_4, VG\_5, VG\_6 & VG\_11). It shows how the  
715 frequency content of the incoming signal can affect the sea-level during many hours after  
716 the seismic rupture.

717           The numerical simulations of the tsunami having followed the Mw 6.4 Les Saintes  
718 earthquake were able to match the witnesses' observations in Les Saintes (Cordrie et al.,  
719 2020). Despite the low resolution (100m) of the present simulation on Les Saintes, there  
720 are some similarities between the two studies of potential impacted zones, for example  
721 in Marigot or Grande Anse Bays. It also shows that other bays, like the ones located





722 between Terre-de-Haut and Ilet à Cabrit, appear to be quite well protected and not  
723 exposed to relatively strong tsunami waves.

724 Finally, this study also highlights the exposed coastline of Dominica: on the north-  
725 northeast coast of the island (Figure 9), 50+ cm waves are simulated, showing that this  
726 island should integrate such a scenario of crustal fault rupture within its tsunami hazard  
727 assessment plan.

728

### 729 **Conclusion**

730 Thanks to HR bathymetry, reflection seismic data and rock/sediment samples, the  
731 analyses of the morphology and tectonic structures of the Marie Galante Basin located in  
732 the middle of the Guadeloupe Archipelago, allow to detail the structural pattern of this  
733 region and to estimate a constant slip rate of *ca.* 0.2 mm.yr<sup>-1</sup> along the Morne Piton Fault  
734 system, cross-cutting the basin, since its inception (*i.e.* over that last 7 Ma). This estimate  
735 divides the previously published estimations of the slip rate by five, and thus increases  
736 the earthquake recurrence time associated to the Morne Piton Fault system from 1Ka to  
737 5-6 Ka. We show that a seismic rupture associated to an earthquake showing a moment  
738 magnitude  $M_w \sim 6.5$  can occur along the Morne Piton Fault system in case of the rupture  
739 of the full length of the fault (all segments being considered connected at depth in the  
740 present demonstration). Such an event would be tsunamigenic according to numerical  
741 simulation results. The multi-segment tsunami modeling illustrates how submarine  
742 morphological and structural features influences the propagation pattern of the tsunami  
743 leading to constructing interferences and resonances, thus increasing the tsunami threat  
744 on nearby islands, especially highlighting a resonance effect within the Les Saintes  
745 Islands, not discussed so far (and potentially the explanation of the 2004 non-reproduced  
746 run-up values). At a regional scale we evidenced that several other regional faults such as  
747 Montserrat-Harvers-Bouillante Fault, Gosier Faut, Karukera Spur border fault, may also  
748 be tsunamigenic. Indeed, although they have the potential to produce relatively low  
749 magnitude ( $<7$ ) earthquakes, their rupture could occur at shallow depth and close to a  
750 highly populated coast. Therefore, scenarii with arc and forearc crustal fault ruptures  
751 must be integrated within their tsunami hazard assessment plan. For that, it is necessary  
752 to have a better knowledge of onshore-offshore structural and seismogenic patterns of  
753 each individual major faults system as the regional low strain rate leads to large



754 recurrence time of tsunamigenic earthquakes (>1000years), *i.e.* much greater than the  
755 historical record.

756

757 ***Competing interests***

758 The contact author has declared that none of the authors has any competing interests.  
759

760 ***Acknowledgements and data***

761 We are grateful to C. Deplus, A. Hirn (IPGP) and M. Laigle (GeoAzur) for providing  
762 Aguadomar and Sismantilles seismic and bathymetry data and to I Thinon and P. Gennoc  
763 (BRGM) for providing the Geoberyx seismic Data. The Kashallow project was supported  
764 by The French National Program DyETI from INSU-CNRS, by the European Interreg IIIB  
765 “Caribbean Space” Fund engaged in Guadeloupe with the EFRD projects (op. 30-700) and  
766 the Region Guadeloupe.

767

768 ***Data availability and request***

769 Litto3D data can be found at <https://diffusion.shom.fr/loisir/litto3d-guad2016.html>  
770 French oceanographic fleet data can be obtain on demand via the Sismer online interface  
771 following the cruise doi – Aguadomar: <https://doi.org/10.17600/98010120>; Sismantilles:  
772 <https://doi.org/10.17600/1080060> and <https://doi.org/10.17600/7010020>; Kashallow:  
773 <https://doi.org/10.17600/9020010>;

774 Requests for the Geoberyx03 data must be adressed to the BRGM.

775 Some figures have been prepared using the Generic Mapping Tools Version 6 software  
776 (Wessel et al., 2019).

777

778

779



780 **References**

781

782 Accary, F., & Roger, J., 2010. Tsunami catalog and vulnerability of Martinique (Lesser  
783 Antilles, France). *Science of Tsunami Hazards*, 29(3).

784 Ajvazi, B., & Czimmer, K., 2019. A comparative analysis of different DEM interpolation  
785 methods in GIS: case study of Rahovec, Kosovo. *Geodesy and cartography*, 45(1), 43-  
786 48. <https://doi.org/10.3846/gac.2019.7921>

787 Arun, P.V., 2013. A comparative analysis of different DEM interpolation methods. *The*  
788 *Egyptian Journal of Remote Sensing and Space Science*, 16(2), 133-139.  
789 <https://doi.org/10.1016/j.ejrs.2013.09.001>

790 Barkan, R. and Ten Brink, U., 2010. Tsunami simulations of the 1867 virgin island earthquake:  
791 Constraints on epicenter location and fault parameters. *Bulletin of the Seismological*  
792 *Society of America*, 100(3), pp.995-1009. <https://doi.org/10.1785/0120090211>

794 Bazin, S., Feuillet, N., Duclos, C., Crawford, W., Nercessian, A., Bengoubou-Valerius, M., ...  
795 & Singh, S. C., 2010. The 2004–2005 Les Saintes (French West Indies) seismic  
796 aftershock sequence observed with ocean bottom seismometers. *Tectonophysics*, 489(1-  
797 4), 91-103. <https://doi.org/10.1016/j.tecto.2010.04.005>

798 Beck, C., Reyss, J.L., Leclerc, F., Moreno, E., Feuillet, N., Barrier, L., Beauducel, F., Boudon,  
799 G., Clément, V., Deplus, C. and Gallou, N., 2012. Identification of deep subaqueous co-  
800 seismic scarps through specific coeval sedimentation in Lesser Antilles: implication for  
801 seismic hazard. *Natural Hazards and Earth System Sciences*, 12(5), pp.1755-1767.  
802 <https://doi.org/10.5194/nhess-12-1755-2012>

803 Bernard, P., & Lambert, J., 1988. Subduction and seismic hazard in the northern Lesser  
804 Antilles: Revision of the historical seismicity. *Bulletin of the Seismological Society of*  
805 *America*, 78(6), 1965-1983.

806 Bernardes, T., Gontijo, I., Andrade, H., Vieira, T.G.C., Alves, H.M.R., 2006. Digital  
807 Terrain Models Derived from SRTM Data and Kriging. In: AbdulRaman A., Zlatanova  
808 S., Coors V. (eds) *Innovations in 3D Geo Information Systems. Lecture Notes in*  
809 *Geoinformation and Cartography*. Springer, Berlin, Heidelberg.  
810 [https://doi.org/10.1007/978-3-540-36998-1\\_51](https://doi.org/10.1007/978-3-540-36998-1_51)

811

812 Bie, L., Rietbrock, A., Hicks, S., Allen, R., Blundy, J., Clouard, V., Collier, J., Davidson, J.,  
813 Garth, T., Goes, S., Harmon, N., Henstock, T., van Huenen, J., Kendall, M., Krüger, F.,



- 814 Lynch, L., Macpherson, C., Robertson, R., Tait, S., Wilknison, J. & Wilson, M., 2020.  
815 Along-arc heterogeneity in local seismicity across the Lesser Antilles subduction zone  
816 from a dense ocean-bottom seismometer network. *Seismological Research Letters*, 91(1),  
817 237-247. <https://doi.org/10.1785/0220190147>
- 818 Biggs, J., & Wright, T. J., 2020. How satellite InSAR has grown from opportunistic science to  
819 routine monitoring over the last decade. *Nature Communications*, 11(1), 1-  
820 4. <https://doi.org/10.1038/s41467-020-17587-6>
- 821 Bilek, S. L. (2010). Invited review paper: Seismicity along the South American subduction  
822 zone: Review of large earthquakes, tsunamis, and subduction zone complexity.  
823 *Tectonophysics*, 495(1-2), 2-14. <https://doi.org/10.1016/j.tecto.2009.02.037>
- 824 Boucard, M., Marcaillou, B., Lebrun, J. F., Laurencin, M., Klingelhoefer, F., Laigle, M.,  
825 Lallemand, S., Schenini, L., Graindorge, D., Cornee, J.J., Münch, P. & Philippon, M.,  
826 2021. Paleogene V-shaped basins and Neogene subsidence of the Northern Lesser  
827 Antilles Forearc. *Tectonics*, 40(3), e2020TC006524.  
828 <https://doi.org/10.1029/2020TC006524>
- 829 Bouysse P., Garrabé F., Mauboussin T., Andreieff P., Battistini R., Carlier P., Hirschberger F.  
830 & Rodet J. (1993). – Carte géologique du département de la Guadeloupe. Notice  
831 explicative: Marie-Galante et îlets de la Petite-Terre, scale 1: 50, 000. – BRGM, Orléans,  
832 France.
- 833 Bouysse, P., Mascle, A. (1994). Sedimentary Basins and Petroleum Plays Around the French  
834 Antilles. In: Mascle, A. (eds) *Hydrocarbon and Petroleum Geology of France*. Special  
835 Publication of the European Association of Petroleum Geoscientists, vol 4. Springer,  
836 Berlin, Heidelberg. [https://doi.org/10.1007/978-3-642-78849-9\\_32](https://doi.org/10.1007/978-3-642-78849-9_32).
- 837 Chadha, R. K., Latha, G., Yeh, H., Peterson, C., & Katada, T. (2005). The tsunami of the great  
838 Sumatra earthquake of M 9.0 on 26 December 2004–Impact on the east coast of India.  
839 *Current Science*, 1297-1301.
- 840 Chen, J. M., Liang, D., & Tang, H. (2012). Interaction between tsunami waves and isolated  
841 conical islands. *Journal of Coastal Research*, 28(5), 1270-1278.
- 842 Colon Useche, S., Clouard, V., Ioualalen, M., Audemard, F. and Monfret, T., 2023. Simulation  
843 of tsunami inundation for the island of Martinique to nearby large earthquakes. *Bulletin*



- 844 of the *Seismological Society of America*, 113(1), pp.252-267.  
845 <https://doi.org/10.1785/0120220093>
- 846 Corbeau, J., Feuillet, N., Lejeune, A. M., Fontaine, F. R., Clouard, V., Saurel, J. M., & OVSM  
847 team, 2021. A significant increase in interplate seismicity near major historical  
848 earthquakes offshore martinique (FWI). *Bulletin of the Seismological Society of*  
849 *America*, 111(6), 3118-3135. <https://doi.org/10.1785/0120200377>
- 850 Cordrie, L., Gailler, A., Escartin, J., Feuillet, N., & Heinrich, P., 2020. Simulation of the 2004  
851 tsunami of Les Saintes in Guadeloupe (Lesser Antilles) using new source constraints.  
852 *Natural Hazards*, 103(2), 2103-2129. <https://doi.org/10.1007/s11069-020-04073-x>
- 853 Cornée, J. J., Leticée, J. L., Münch, P., Quillevere, F., Lebrun, J. F., Moissette, P., Braga, C.,  
854 Melinte-Dobrinescu, M., De Min, L., Oudet, J. & Randrianasolo, A., 2012.  
855 Sedimentology, palaeoenvironments and biostratigraphy of the Pliocene–Pleistocene  
856 carbonate platform of Grande-Terre (Guadeloupe, Lesser Antilles forearc).  
857 *Sedimentology*, 59(5), 1426-1451. <https://doi.org/10.1111/j.1365-3091.2011.01311.x>
- 858 Cornée, J. J., Münch, P., Philippon, M., Boudagher-Fadel, M., Quillévééré, F., Melinte-  
859 Dobrinescu, M., Lebrun, J.F., Meyer, S., Montheil, L., Lallemand, S., Marcaillou, B.,  
860 Laurencin, M., Legendre, L., Garroq, C., Boucard, M., Beslier, M.O., Laigle, M.,  
861 Schenini, L., Fabre, P.H. & Marivaux, L., 2021. Lost islands in the northern Lesser  
862 Antilles: possible milestones in the Cenozoic dispersal of terrestrial organisms between  
863 South-America and the Greater Antilles. *Earth-Science Reviews*, 217, 103617.  
864 <https://doi.org/10.1016/j.earscirev.2021.103617>
- 865 Cornée, J.J., De Min, L., Lebrun, J.F., Quillévééré, F., Melinte-Dobrinescu, M., BouDagher-  
866 Fadel, M., Montheil, L. , Marcaillou, B., Thinon, I. and Philippon M., 2023.  
867 Paleogeographic evolution and vertical motion of the central Lesser Antilles forearc since  
868 the Early Miocene: A potential driver for land fauna dispersals between the americas.  
869 *Marine and Petroleum Geology*, 152, 106264.  
870 <https://doi.org/10.1016/j.marpetgeo.2023.106264>
- 871 Dao, M. H., & Tkalich, P., 2007. Tsunami propagation modelling—a sensitivity study. *Natural*  
872 *Hazards and Earth System Sciences*, 7(6), 741-754. [https://doi.org/10.5194/nhess-7-741-](https://doi.org/10.5194/nhess-7-741-2007)  
873 [2007](https://doi.org/10.5194/nhess-7-741-2007)
- 874 Delpy, M., Lastiri, X., Abadie, S., Roeber, V., Maron, P., Liria, P., & Mader, J. (2021).  
875 Characterization of the wave resource variability in the French Basque coastal area based  
876 on a high-resolution hindcast. *Renewable Energy*, 178, 79-95.  
877 <https://doi.org/10.1016/j.renene.2021.05.167>



- 878 DeMets, C., Jansma, P. E., Mattioli, G. S., Dixon, T. H., Farina, F., Bilham, R., Calais, E. &  
879 Mann, P., 2000. GPS geodetic constraints on Caribbean-North America plate motion.  
880 Geophysical Research Letters, 27(3), 437-440. <https://doi.org/10.1029/1999GL005436>
- 881 De Min, L., 2014. Sismo-stratigraphie multi-échelles d'un bassin d'avant-arc: le bassin de  
882 Marie-Galante, Petites Antilles(Doctoral dissertation, Antilles-Guyane).
- 883 De Min, L., Lebrun, J. F., Cornée, J. J., Münch, P., Léticée, J. L., Quillévéré, F., Melinte-  
884 Dobrinescu, M., Randrianasolo, A., Marcaillou, B. & Zami, F., 2015. Tectonic and  
885 sedimentary architecture of the Karukéra spur: A record of the Lesser Antilles fore-arc  
886 deformations since the Neogene. *Marine Geology*, 363, 15-37.  
887 <https://doi.org/10.1016/j.margeo.2015.02.007>
- 888 Deplus C., 1998, AGUADOMAR cruise, RV L'Atalante, <https://doi.org/10.17600/98010120>
- 889 Dix, C.H., 1955. Seismic Velocities from Surface Measurements," *Geophysics* 20, no. 1, 68-  
890 86. <https://doi.org/10.1190/1.1438126>
- 891 do Carmo, J. S. A. (2022). Dominant processes that amplify the swell towards the coast: the  
892 Nazaré Canyon and the giant waves. *Research, Society and Development*, 11(11),  
893 e578111133804-e578111133804. <https://doi.org/10.33448/rsd-v11i11.33804>
- 894 Escartín, J., Leclerc, F., Olive, J. A., Mevel, C., Cannat, M., Petersen, S., Augustin, N., Feuillet,  
895 N., Deplus, C., Bezos, A., Bonnemains, D., Chavagnac, V., Choi, Y., Godard, M., Haaga,  
896 K., Hamelin, C., Ildefonse, B., Jamieson, J.W., John, B.E., Leleu, T., MacLead, C.J.,  
897 Massot-Campos, M., Nomikou, P., Paquet, M., Tominaga, M., Triebe, L., Campos, R.,  
898 Gracias, N., Garcia, R., Andreani, M. & Vilaseca, G. (2016). First direct observation of  
899 coseismic slip and seafloor rupture along a submarine normal fault and implications for  
900 fault slip history. *Earth and Planetary Science Letters*, 450, 96-  
901 107.<https://doi.org/10.1016/j.epsl.2016.06.024>
- 902 Escartin, J., Leclerc, F., Nathalie, F., Le Friant, A., Billant, J., Olive, J. A. L., Henri, M.,  
903 Andreani, M., Arnaubec, A., Dano, A., Delorme, A., Deplus, C., Fournasson, M.L., Gini,  
904 C., Gracias, N., Hamelin, C., Istenic, K., Komorowski, J.C., Marchand C., Mevel, C.,  
905 Onstad, S., Quidelleur, X. & Garcia, R. (2018, December). Mapping the Mw6.3 2004  
906 Les Saintes earthquake seafloor rupture with deep-sea vehicles: Length, displacement,  
907 nature, and links between coseismic deformation and erosion/sedimentation. In *AGU Fall*  
908 *Meeting Abstracts* (Vol. 2018, pp. EP51D-1851).
- Feuillet, N., 2000. Sismotectonique des Petites Antilles: Liaison entre activité sismique et  
volcanique (Doctoral dissertation, Paris 7).



- 909 Feuillet, N., Manighetti, I., & Tapponnier, P., 2001. Extension active perpendiculaire à la  
910 subduction dans l'arc des Petites Antilles (Guadeloupe, Antilles françaises). *Comptes*  
911 *Rendus de l'Académie des Sciences-Series IIA-Earth and Planetary Science*, 333(9), 583-  
912 590.
- 913 Feuillet, N., Manighetti, I., Tapponnier, P., & Jacques, E., 2002. Arc parallel extension and  
914 localization of volcanic complexes in Guadeloupe, Lesser Antilles. *Journal of*  
915 *Geophysical Research: Solid Earth*, 107(B12), ETG-3.  
916 <https://doi.org/10.1029/2001JB000308>
- 917 Feuillet, N., Tapponnier, P., Manighetti, I., Villemant, B., & King, G. C. P., 2004. Differential  
918 uplift and tilt of Pleistocene reef platforms and Quaternary slip rate on the Morne-Piton  
919 normal fault (Guadeloupe, French West Indies). *Journal of Geophysical Research: Solid*  
920 *Earth*, 109(B2). <https://doi.org/10.1029/2003JB002496>
- 921 Feuillet, N., Leclerc, F., Tapponnier, P., Beauducel, F., Boudon, G., Le Friant, A., Deplus, C.,  
922 Lebrun, J.F., Nercessian, A., Saurel, J.M. & Clément, V., 2010. Active faulting induced  
923 by slip partitioning in Montserrat and link with volcanic activity: New insights from the  
924 2009 GWADASEIS marine cruise data. *Geophysical Research Letters*, 37(19).  
925 <https://doi.org/10.1029/2010GL042556>
- 926 Feuillet, N., Beauducel, F., & Tapponnier, P., 2011. Tectonic context of moderate to large  
927 historical earthquakes in the Lesser Antilles and mechanical coupling with volcanoes.  
928 *Journal of Geophysical Research: Solid Earth*, 116(B10).  
929 <https://doi.org/10.1029/2011JB008443>
- 930 Fujita, M., Ishikawa, T., Mochizuki, M., Sato, M., Toyama, S. I., Katayama, M., Kawai, K.,  
931 Mastumoto, Y., Yabuki, T., Asada, A. & Colombo, O. L., 2006. GPS/Acoustic seafloor  
932 geodetic observation: method of data analysis and its application. *Earth, planets and*  
933 *space*, 58(3), 265-275. <https://doi.org/10.1186/BF03351923>
- 934 GEBCO Compilation Group, 2021. GEBCO 2021 Grid (doi:10.5285/c6612cbe-50b3-0cff-  
935 e053-6c86abc09f8f)
- 936 Geli, L., Çağatay, N., Gasperini, L., Favali, P., Henry, P., & Çifçi, G., 2011. ESONET WP4-  
937 Demonstration Missions. MARMARA-DM final report.  
938 <https://archimer.ifremer.fr/doc/00032/14324/>
- 939 Goldfinger, C., Nelson, C. H., Morey, A. E., Johnson, J. E., Patton, J. R., Karabanov, E. B.,  
940 Gutierrez-Pastor, J., Eriksson, A.T., Gracia, E., Dunhill, G., Enkin, R.J., Dallimore, A.  
941 & Vallier, T., 2012. Turbidite event history—Methods and implications for Holocene





- 942 paleoseismicity of the Cascadia subduction zone(No. 1661-F). US Geological Survey.  
943 <https://doi.org/10.3133/pp1661F>
- 944 Gonzalez, O.L., Clouard, V., & Zahradnik, J., 2017. Moment tensor solutions along the central  
945 Lesser Antilles using regional broadband stations. *Tectonophysics*, 717, 214-225.  
946 <https://doi.org/10.1016/j.tecto.2017.06.024>
- 947 Gusman, A.R., Supendi, P., Nugraha, A.D., Power, W., Latief, H., Sunendar, H., Widiyantoro,  
948 S., Daryono, Wiyono, S.H., Hakim, A., Muhari, A., Wang, X., Burbidge, D., Palgunadi,  
949 K., Hamling, I., Daryono, M.R., 2019. Source model for the tsunami inside Palu Bay  
950 following the 2018 Palu earthquake, Indonesia. *Geophysical Research Letters*, 46, 8721-  
951 8730, <https://doi.org/10.1029/2019GL082717>.
- 952 Gusman, A.R., Roger, J., Power, W., Fry, B., Kaneko, Y., 2022. The 2021 Loyalty Islands  
953 earthquake (Mw7.7): Tsunami waveform inversion and implications for tsunami  
954 forecasting for New Zealand. *Earth and Space Science*, e2022EA002346,  
955 <https://doi.org/10.1029/2022EA002346>.
- 956 Gutscher, M. A., Royer, J. Y., Graindorge, D., Murphy, S., Klingelhoefer, F., Aiken, C.,  
957 Cattaneo, A., Barreca, G., Quétel, L., Riccobene, G., Petersen, F., Urlaub, M., Krastel,  
958 S., Gross, F., Kopp, H., Margheriti, L. Beranzoli, L., 2019. Fiber optic monitoring of  
959 active faults at the seafloor: I the FOCUS project. *Photoniques*, 32-37.  
960 <https://doi.org/10.1051/photon/2019S432>
- 961 Hirata, K., Aoyagi, M., Mikada, H., Kawaguchi, K., Kaiho, Y., Iwase, R., Morita, S., Fujisawa,  
962 I., Sugioka, H., Mitsuzawa, K., Suyehiro, K. & Fujiwara, N., 2002. Real-time  
963 geophysical measurements on the deep seafloor using submarine cable in the southern  
964 Kurile subduction zone. *IEEE Journal of Oceanic Engineering*, 27(2), 170-181.  
965 <https://doi.org/10.1109/JOE.2002.1002471>
- 966 IOC-UNESCO (2020). Experts Meeting on Sources of Tsunamis in the Lesser Antilles Fort-  
967 de-France, Martinique (France) 18–20 March 2019. Workshop Reports, (291), 55p. Open  
968 Access version : <https://archimer.ifremer.fr/doc/00665/77736/>
- 969 Kido, M., Fujimoto, H., Miura, S., Osada, Y., Tsuka, K., & Tabei, T., 2006. Seafloor  
970 displacement at Kumano-nada caused by the 2004 off Kii Peninsula earthquakes,  
971 detected through repeated GPS/Acoustic surveys. *Earth, planets and space*, 58(7), 911-  
972 915. <https://doi.org/10.1186/BF03351996>
- 973 Kopp, H., Weinzierl, W., Becel, A., Charvis, P., Evain, M., Flueh, E. R., Gailler, A., Galve, A.,  
974 Hirn, A., Kandilarov, D., Klaeschen, D., Laigle, M., Papenberg, C., Planert, L. & Roux,  
975 E., 2011. Deep structure of the central Lesser Antilles Island Arc: relevance for the



- 976 formation of continental crust. *Earth and Planetary Science Letters*, 304(1-2), 121-134.  
977 <https://doi.org/10.1016/j.epsl.2011.01.024>
- 978 Laigle M., Lebrun J.-F., Hirn A. (2007) SISMANTILLES 2 cruise, RV L'Atalante,  
979 <https://doi.org/10.17600/7010020>
- 980 Lander, J. F., & Whiteside, L. S., 1997. Caribbean tsunamis: an initial history. In *Caribbean*  
981 *Tsunami Workshop*, June (pp. 11-13).
- 982 Lander, J. F., Whiteside, L. S., & Lockridge, P. A., 2003. Two decades of global tsunamis.  
983 *Science of Tsunami Hazards*, 21(1), 3.
- 984 Lardeaux, J. M., Münch, P., Corsini, M., Cornée, J. J., Verati, C., Lebrun, J. F., Guillevere, F.,  
985 Melinte-Dobrinescu, M., Leticee, J.L., Fietzke, J., Mazabraud, Y., Cordrey, F. &  
986 Randrianasolo, A., 2013. La Désirade island (Guadeloupe, French West Indies): a key  
987 target for deciphering the role of reactivated tectonic structures in Lesser Antilles arc  
988 building. *Bulletin de la Société géologique de France*, 184(1-2), 21-34.  
989 <https://doi.org/10.2113/gssgfbull.184.1-2.21>
- 990 Laurencin, M., Graindorge, D., Klingelhoefer, F., Marcaillou, B., & Evain, M., 2018. Influence  
991 of increasing convergence obliquity and shallow slab geometry onto tectonic deformation  
992 and seismogenic behavior along the Northern Lesser Antilles zone. *Earth and Planetary*  
993 *Science Letters*, 492, 59-72. <https://doi.org/10.1029/2019GL083490>
- 994 Lebrun, J.-F., Cornée, J.-J., Münch, P., Guennoc, P., Thinon, I., Begot, J., Mazabraud, Y.,  
995 Fournier, F., Feuillet, N., Randrianasolo, A., 2008. La Mission KaShallow 1 - N/O Antéa  
996 - 26 avril - 05 Mai - Sismique réflexion haute résolution dans le bassin de Marie-Galante  
997 - Avant-arc des Petites Antilles. Rapport de l'Université des Antilles et de la Guyane.
- 998 Leclerc, F., Feuillet, N., & Deplus, C., 2016. Interactions between active faulting, volcanism,  
999 and sedimentary processes at an island arc: Insights from Les Saintes channel, Lesser  
1000 Antilles arc. *Geochemistry, Geophysics, Geosystems*, 17(7), 2781-2802.  
1001 <https://doi.org/10.1002/2016GC006337>
- 1002 Le Friant, A., Heinrich, P., & Boudon, G., 2008. Field survey and numerical simulation of the  
1003 21 November 2004 tsunami at Les Saintes (Lesser Antilles). *Geophysical Research*  
1004 *Letters*, 35(12). <https://doi.org/10.1029/2008GL034051>
- 1005 Legendre, L., Philippon, M., Münch, P., Leticee, J. L., Noury, M., Maincent, G., Cornée, J.J.,  
1006 Caravati, A., Lebrun, J.F. & Mazabraud, Y., 2018. Trench bending initiation: Upper plate  
1007 strain pattern and volcanism. insights from the Lesser Antilles arc, St. Barthelemy island,  
1008 French West Indies. *Tectonics*, 37(9), 2777-2797.



- 1009 Lehu, R., Lallemand, S., Ratzov, G., Babonneau, N., Hsu, S. K., Lin, A. T., & Dezileau, L.,  
1010 2016. An attempt to reconstruct 2700 years of seismicity using deep-sea turbidites  
1011 offshore eastern Taiwan. *Tectonophysics*, 692, 309-324.  
1012 <https://doi.org/10.1016/j.tecto.2016.04.030>
- 1013 Leticee, J. L., Cornee, J. J., Münch, P., Fietzke, J., Philippon, M., Lebrun, J. F., De Min, L., &  
1014 Randrianasolo, A., 2019. Decreasing uplift rates and Pleistocene marine terraces  
1015 settlement in the central lesser Antilles fore-arc (La Désirade Island, 16° N). *Quaternary*  
1016 *International*, 508, 43-59. <https://doi.org/10.1016/j.quaint.2018.10.030>
- 1017 Lewis, K. B. (1980). Quaternary sedimentation on the Hikurangi oblique-subduction and  
1018 transform margin, New Zealand. *Sedimentation in oblique-slip mobile zones*, 171-189.  
1019 <https://doi.org/10.1002/9781444303735.ch10>
- 1020 Liu, P.L.F., Woo, S.B., Cho, Y.S., 1998. Computer programs for tsunami propagation and  
1021 inundation. Ithaca (NY): Cornell University. Technical Report.
- 1022 Mallet, R., 1853. Catalogue of Recorded Earthquakes from 1606 B.C. to A.D. 1850, Part  
1023 I, 1606 B.C. to 1755 A.D. Report of the 22nd Meeting of the British Association for the  
1024 Advancement of Science, held in Belfast, Sept. 1852, John Murray, London, 177 pp.
- 1025 Mallet R. (1854). Catalogue of Recorded Earthquakes from 1606 B.C. to A.D. 1850, Part II,  
1026 1755 A.D. to 1784 A.D., Report of the 23rd meeting of the British Association for the  
1027 Advancement of Science, held in Hull, Sept. 1853, John Murray, London, 118-212.
- 1028 Mallet R. (1855). Catalogue of Recorded Earthquakes from 1606 B.C. to A.D. 1850, Part III,  
1029 1784 A.D. to 1842 A.D., Report of the 24th Meeting of the British Association for the  
1030 Advancement of Science, John Murray, London, 326 pp.
- 1031 Martins, I., Vitorino, J., & Almeida, S. (2010, May). The Nazare Canyon observatory (W  
1032 Portugal) real-time monitoring of a large submarine canyon. In *OCEANS'10 IEEE*  
1033 *SYDNEY* (pp. 1-7). IEEE.
- 1034 Martínez-Lorienté, S., Sallarès, V., & Gràcia, E., 2021. The Horseshoe Abyssal plain Thrust  
1035 could be the source of the 1755 Lisbon earthquake and tsunami. *Communications earth*  
1036 *& environment*, 2(1), 145. <https://doi.org/10.1038/s43247-021-00216-5>
- 1037 Massin, F., Clouard, V., Vorobieva, I., Beauducel, F., Saurel, J. M., Satriano, C., Bouin,  
1038 M. P., & Bertil, D. (2021). Automatic picking and probabilistic location for earthquake  
1039 assessment in the lesser antilles subduction zone (1972-2012). In *Comptes Rendus -*  
1040 *Geoscience* (Vol. 353, Issue S1). Academie des sciences.  
1041 <https://doi.org/10.5802/crgeos.81>. <https://doi.org/10.5802/crgeos.81>
- 1042 McCalpin, J.P. 1996. (Ed.), *Paleoseismology*, Academic Press, London, p. 583



- 1043 Münch, P., Lebrun, J. F., Cornée, J. J., Thinon, I., Guennoc, P., Marcaillou, B. J., Begot, J.,  
1044 Bertrand, G., Bes De Berc, S., Biscarrat, K., Claud, C., De Min, L., Fournier, F., Gailler,  
1045 L., Grandorge, D., Leticee, J.L., Marie, L., Mazabraud, Y., Melinte-Dobrinescu, M.,  
1046 Moissette, P., Quilevere, F., Verati, C. & Randrianasolo, A., 2013. Pliocene to Pleistocene  
1047 carbonate systems of the Guadeloupe archipelago, French Lesser Antilles: a land and sea  
1048 study (the KaShallow project). *Bulletin de la Société géologique de France*, 184(1-2), 99-  
1049 110. <https://doi.org/10.2113/gssgfbull.184.1-2.99>
- 1050 Münch, P., Cornee, J. J., Lebrun, J. F., Quillevere, F., Verati, C., Melinte-Dobrinescu, M.,  
1051 Demory, B., Smith, F., Jourdan, J.M., Lardeaux, J.M., De Min, L., Leticee, J.L. &  
1052 Randrianasolo, A., 2014. Pliocene to Pleistocene vertical movements in the forearc of the  
1053 Lesser Antilles subduction: insights from chronostratigraphy of shallow-water carbonate  
1054 platforms (Guadeloupe archipelago). *Journal of the Geological Society*, 171(3), 329-341.  
1055 <https://doi.org/10.1144/jgs2013-005>
- 1056 NASA Shuttle Radar Topography Mission (SRTM)(2013). Shuttle Radar Topography Mission  
1057 (SRTM) Global. Distributed by OpenTopography. <https://doi.org/10.5069/G9445JDF>.  
1058 Accessed: 2022-12-07.
- 1059 Nikolkina, I., Zahibo, N., & Pelinovsky, E., 2010. Tsunami in Guadeloupe (Caribbean Sea).  
1060 *The Open Oceanography Journal*, 4(1). <https://doi.org/10.2174/1874252101004010044>
- 1061 Okada, Y., 1985. Surface deformation due to shear and tensile faults in a half-space. *Bulletin*  
1062 *of the seismological society of America*, 75(4), 1135-1154.  
1063 <https://doi.org/10.1785/BSSA0750041135>
- 1064 O'loughlin, K. F., & Lander, J. F., 2003. Caribbean tsunamis: a 500-year history from 1498-  
1065 1998 (Vol. 20). Springer Science & Business Media.
- 1066 Padron, C., Klingelhoefer, F., Marcaillou, B., Lebrun, J. F., Lallemand, S., Garroq, C., Laigle,  
1067 M., Roest, W.R., Beslier, M.O., Schenini, L., Graindorge, D., Gay, A., Audemard, F.,  
1068 Münch, P. & GARANTI Cruise Team., 2021. Deep structure of the Grenada Basin from  
1069 wide-angle seismic, bathymetric and gravity data. *Journal of Geophysical Research:*  
1070 *Solid Earth*, 126(2), e2020JB020472. <https://doi.org/10.1029/2020JB020472>
- 1071 Paris, R., Sabatier, P., Biguenet, M., Bougouin, A., André, G., Roger, J., 2021. A tsunami  
1072 deposit at Anse Meunier, Martinique Island : evidence of the 1755 CE Lisbon tsunami  
1073 and implication for hazard assessment. *Marine Geology*, 439, 106561,  
1074 <https://doi.org/10.1016/j.margeo.2021.106561>.



- 1075 Petersen, F., Kopp, H., Lange, D., Hannemann, K., & Urlaub, M., 2019. Measuring tectonic  
1076 seafloor deformation and strain-build up with acoustic direct-path ranging. *Journal of*  
1077 *Geodynamics*, 124, 14-24. <https://doi.org/10.1016/j.jog.2019.01.002>
- 1078 Philippon, M., & Corti, G., 2016. Obliquity along plate boundaries. *Tectonophysics*, 693, 171-  
1079 182. <https://doi.org/10.1016/j.tecto.2016.05.033>
- 1080 Prasetya, G., Beavan, J., Wang, X., Reyners, M., Power, W., Wilson, K., Lukovic, B., 2011.  
1081 Evaluation of the 15 July 2009 Fjorland, New Zealand tsunami in the source region. *Pure*  
1082 *and Applied Geophysics*, 168, 1973-1987, <https://doi.org/10.1007/s00024-011-0282-6>.
- 1083 Roger, J., Allgeyer, S., Hébert, H., Baptista, M. A., Loevenbruck, A., & Schindelé, F., 2010.  
1084 The 1755 Lisbon tsunami in Guadeloupe Archipelago: source sensitivity and  
1085 investigation of resonance effects. *The Open Oceanography Journal*, 4(1).  
1086 <https://doi.org/10.2174/1874252101004010058>
- 1087 Roger, J., Baptista, M. A., Sahal, A., Accary, F., Allgeyer, S., & Hébert, H., 2011. The  
1088 transoceanic 1755 Lisbon tsunami in Martinique. *Pure and Applied Geophysics*, 168(6),  
1089 1015-1031. <https://doi.org/10.1007/s00024-010-0216-8>
- 1090 Roger, J., Dudon, B., & Zahibo, N., 2013. Tsunami hazard assessment of Guadeloupe Island  
1091 (FWI) related to a megathrust rupture on the Lesser Antilles subduction interface. *Natural*  
1092 *Hazards and Earth System Sciences*, 13(5), 1169-1183. [https://doi.org/10.5194/nhess-13-](https://doi.org/10.5194/nhess-13-1169-2013)  
1093 1169-2013
- 1094 Roger, J., Pelletier, B., & Aucan, J. (2019). Update of the tsunami catalogue of New Caledonia  
1095 using a decision table based on seismic data and marigraphic records. *Natural Hazards*  
1096 *and Earth System Sciences*, 19(7), 1471-1483. [https://doi.org/10.5194/nhess-19-1471-](https://doi.org/10.5194/nhess-19-1471-2019)  
1097 2019
- 1098 Roger, J., Pelletier, B., Gusman, A., Power, W., Wang, X., Burbidge, D., & Duphil, M., 2023.  
1099 Potential tsunami hazard of the southern Vanuatu Subduction Zone: tectonics, case study  
1100 of the Matthew Island tsunami of 10 February 2021 and implication in regional hazard  
1101 assessment. *Natural Hazards and Earth System Sciences*, 23(2), 393-414,  
1102 <https://doi.org/10.5194/nhess-23-393-2023>.
- 1103 Ruiz, M., Galve, A., Monfret, T., Sapin, M., Charvis, P., Laigle, M., Evain, M., Hirn, A., Flueh,  
1104 E., Gallart, K., Diaz, J., Lebrun, J.F. & Lebrun, J. F., 2013. Seismic activity offshore  
1105 Martinique and Dominica islands (Central Lesser Antilles subduction zone) from  
1106 temporary onshore and offshore seismic networks. *Tectonophysics*, 603, 68-78.  
1107 <https://doi.org/10.1016/j.tecto.2011.08.006>



- 1108 Salichon, J., Lemoine, A., Aochi, H., 2009. Validation of teleseismic inversion of the 2004  
1109 Mw 6.3 Les Saintes, Lesser Antilles, earthquake by 3D finite-difference forward  
1110 modelling. *Bull. Seismol. Soc. Am.* 99, 3390–3401. <https://doi.org/10.1785/0120080315>
- 1111 Satake, K., & Tanioka, Y., 1999. Sources of tsunami and tsunamigenic earthquakes in  
1112 subduction zones. *Pure and Applied Geophysics*, 154(3), 467–483.  
1113 <https://doi.org/10.1785/0120120306>
- 1114 Seibert, C., Feuillet, N., Ratzov, G., Beck, C., & Cattaneo, A., 2020. Seafloor morphology and  
1115 sediment transfer in the mixed carbonate-siliciclastic environment of the Lesser Antilles  
1116 forearc along Barbuda to St. Lucia. *Marine Geology*, 428, 106242.  
1117 <https://doi.org/10.1016/j.margeo.2020.106242>
- 1118 Symithe, S. J., Calais, E., Haase, J. S., Freed, A. M., & Douilly, R., 2013. Coseismic slip  
1119 distribution of the 2010 M 7.0 Haiti earthquake and resulting stress changes on regional  
1120 faults. *Bulletin of the Seismological Society of America*, 103(4), 2326–2343.  
1121 <https://doi.org/10.1785/0120120306>
- 1122 ten Brink, U., Danforth, W., Polloni, C., Andrews, B., Llanes, P., Smith, S., Parker, E., and  
1123 Uozumi, T. 2004. New seafloor map of the Puerto Rico trench helps assess earthquake  
1124 and tsunami hazards. *Eos, Transactions American Geophysical Union* 85: 349–360.  
1125 doi:10.1029/2004EO370001.
- 1126 Terrier, M., Combes P. avec la collaboration de D. Carbon, B. Grellet, O. Sedan (2002) -  
1127 FAILLES ACTIVES ET EVALUATION DE L’ALEA SISMIQUE : Prise en compte  
1128 des failles actives dans l’aménagement du territoire aux Antilles (Martinique et  
1129 Guadeloupe). Partie 1 : Identification des systèmes de failles actives dans l’archipel de la  
1130 Guadeloupe et l’île de la Martinique. Rapport BRGM/RP-51258-FR. 118 pages. 30  
1131 figures. 8 tableaux. 4 annexes
- 1132 Thingbaijam, K.K.S., Mai, P.M. and Goda, K., 2017. New Empirical Earthquake Source-  
1133 Scaling Laws New Empirical Earthquake Source-Scaling Laws. *Bulletin of the*  
1134 *Seismological Society of America*, 107(5), pp.2225-2246.  
1135 <https://doi.org/10.1785/0120170017>
- 1136 Thinon, I, Bitri, A., 2003. GEOBERYX03 cruise, RV Beryx, [Catalogue des campagnes à la](http://www.flotteoceanographique.fr)  
1137 [mer \(flotteoceanographique.fr\)](http://www.flotteoceanographique.fr) ;browsed on-line on Seadatanet webportal  
1138 (SISM\_BGM\_FI352003000010, <https://cdi.seadatanet.org/>);
- 1139 Thinon I., Bitri A., Guennoc P. & Truffert C. (2004). – Levés sismique et magnétique du  
1140 plateau occidental de l’île de Basse-Terre, Guadeloupe (Campagne Geoberyx03).



- 1141 Apports à la compréhension du contexte structural du champ géothermique de Bouillante.  
1142 – BRGM/RP-53152-FR, 77.
- 1143 Thinon, I., Guennoc, P., Bitri, A., Truffert C., 2010, Study of the Bouillante Bay (West Basse-  
1144 Terre Island shelf): contribution of geophysical surveys to the understanding of the  
1145 structural context of Guadeloupe (French West Indies - Lesser Antilles). Bull. Soc. Geol.  
1146 Fr., 181, 51-65, <http://doi.org/10.2113/gssgfbull.181.1.51>
- 1147 TL/ICMMG (2023). Global Historical Tsunami Database. Institute of Computational  
1148 Mathematics and Mathematical Geophysics SB RAS Tsunami Laboratory, Novosibirsk,  
1149 Russia, <http://tsun.sscc.ru/gtdb/default.aspx> (last accessed on 1 February 2023).
- 1150 Tronin, A. A., 2009. Satellite remote sensing in seismology. A review. Remote Sensing, 2(1),  
1151 124-150. <https://doi.org/10.3390/rs2010124>
- 1152 van Rijnsingen, E. M., Calais, E., Jolivet, R., de Chabaliér, J. B., Jara, J., Symithe, S., ... & Ryan,  
1153 G. A., 2021. Inferring interseismic coupling along the lesser antilles arc: A Bayesian  
1154 approach. Journal of Geophysical Research: Solid Earth, 126(2), e2020JB020677.  
1155 <https://doi.org/10.1029/2020JB020677>
- 1156 Wallace, T. C., Helmburger, D. V., & Ebel, J. E., 1981. A broadband study of the 13 August  
1157 1978 Santa Barbara earthquake. *Bulletin of the Seismological Society of America*, 71(6),  
1158 1701-1718. <https://doi.org/10.1785/BSSA0710061701>
- 1159 Wang, X., 2008. Numerical modelling of surface and internal waves over shallow and  
1160 intermediate water [PhD thesis]. Ithaca (NY): Cornell University. 245 p.
- 1161 Wang, X., Power, W.L., 2011. COMCOT: a tsunami generation, propagation and run-up  
1162 model. Lower Hutt (NZ): GNS Science. 121 p. (GNS Science report; 2011/43).
- 1163 Wang X, Lukovic B, Power WL, Mueller C., 2017. High-resolution inundation modelling with  
1164 explicit buildings. Lower Hutt (NZ): GNS Science. 27 p. (GNS Science report 2017/13).  
1165 <https://doi.org/10.21420/G2RW2N>.
- 1166 Wells, D. L., & Coppersmith, K. J., 1994. New empirical relationships among magnitude,  
1167 rupture length, rupture width, rupture area, and surface displacement. Bulletin of the  
1168 seismological Society of America, 84(4), 974-1002.  
1169 <https://doi.org/10.1785/BSSA0840040974>
- 1170 Wessel, P., Luis, J.F., Uieda, L., Scharroo, R., Wobbe, F., Smith, W.H.F., Tian, D., 2019. The  
1171 Generic Mapping Tools Version 6. *Geochemistry, Geophysics, Geosystems*, 20(11),  
1172 5556-5564, <https://doi.org/10.1029/2019GC008515>.

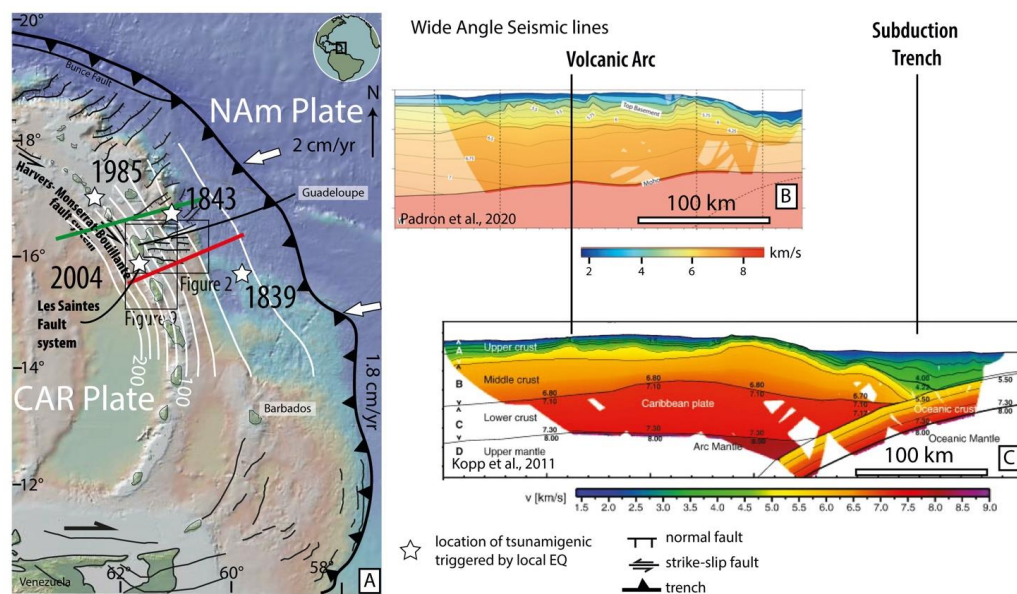




- 1173 Yamazaki, Y., Cheung, K. F., & Lay, T., 2013. Modeling of the 2011 Tohoku near-field  
1174 tsunami from finite-fault inversion of seismic waves. *Bulletin of the Seismological*  
1175 *Society of America*, 103(2B), 1444-1455. <https://doi.org/10.1785/0120120103>  
1176 Zahibo, N., Pelinovsky, E., Kurkin, A., & Kozelkov, A., 2003. Estimation of far-field tsunami  
1177 potential for the Caribbean Coast based on numerical simulation. *Science of Tsunami*  
1178 *Hazards*, 21(4), 202-222.  
1179 Zahibo, N., Pelinovsky, E., Okal, E., Yalçiner, A., Kharif, C., Talipova, T., & Kozelkov, A.,  
1180 2005. The earthquake and tsunami of November 21, 2004 at Les Saintes, Guadeloupe,  
1181 Lesser Antilles. *Science of Tsunami Hazards*, 23(1), 25-39.  
1182 Zhang, L., Baba, K., Liang, P., Shimizu, H., & Utada, H., 2014. The 2011 Tohoku Tsunami  
1183 observed by an array of ocean bottom electromagnetometers. *Geophysical Research*  
1184 *Letters*, 41(14), 4937-4944. <https://doi.org/10.1002/2014GL060850>  
1185

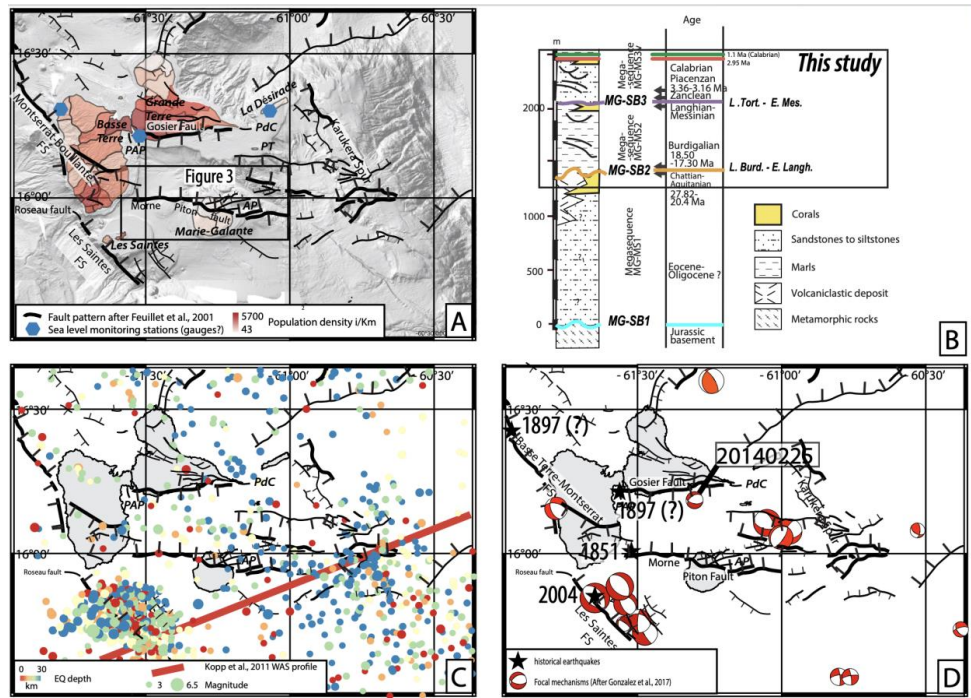


1186 FIGURES



1187

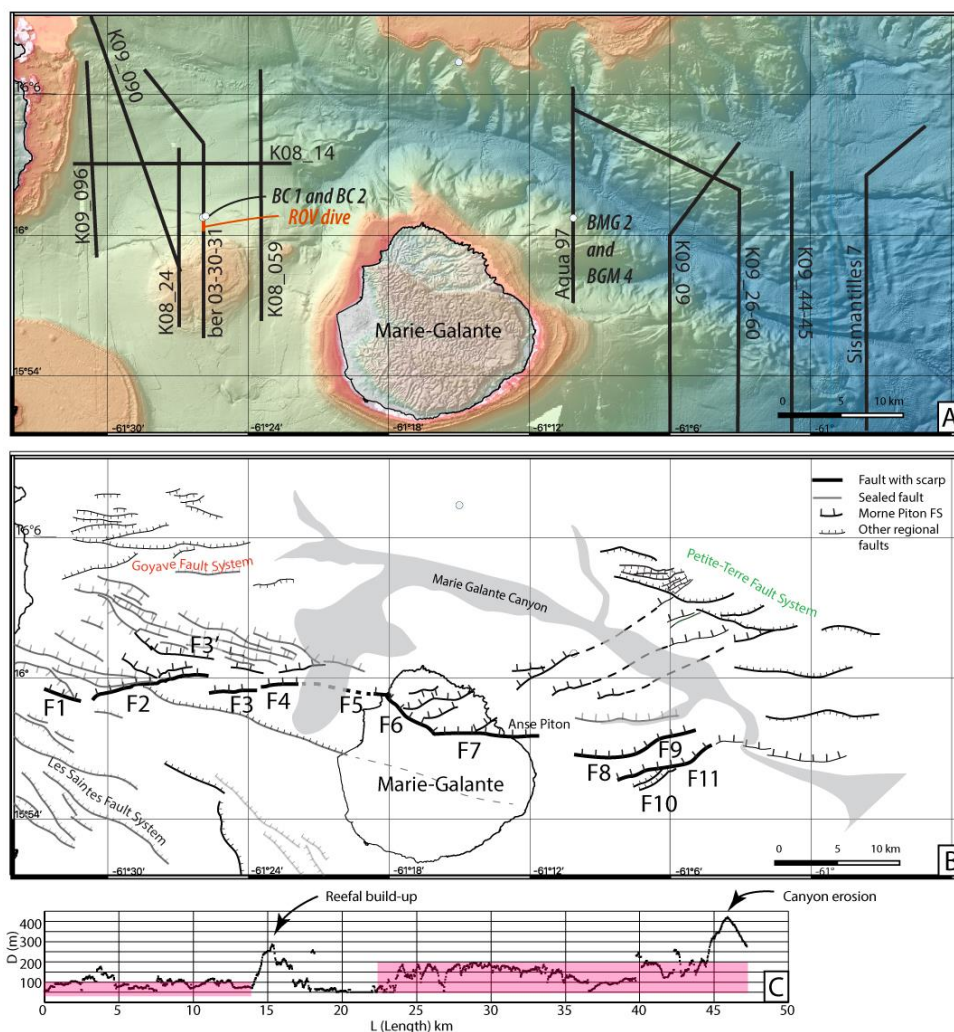
1188 *Figure 1: A: Synthetic tectonic map of the Lesser Antilles forearc. Structures after Feuillet et*  
 1189 *al. (2002), De Min (2014), Laurencin et al. (2019), Legendre (2018), Boucard et al. (2021).*  
 1190 *Red and green thick lines indicate location of the Wide Angle Seismic lines from B. Kopp et*  
 1191 *al. (2011) and C. Padron et al. (2021) respectively. White Star: location of tsunamigenic*  
 1192 *earthquakes. Thick white contour lines: Slab depth isocontour from Bie et al. (2020).*  
 1193



1194

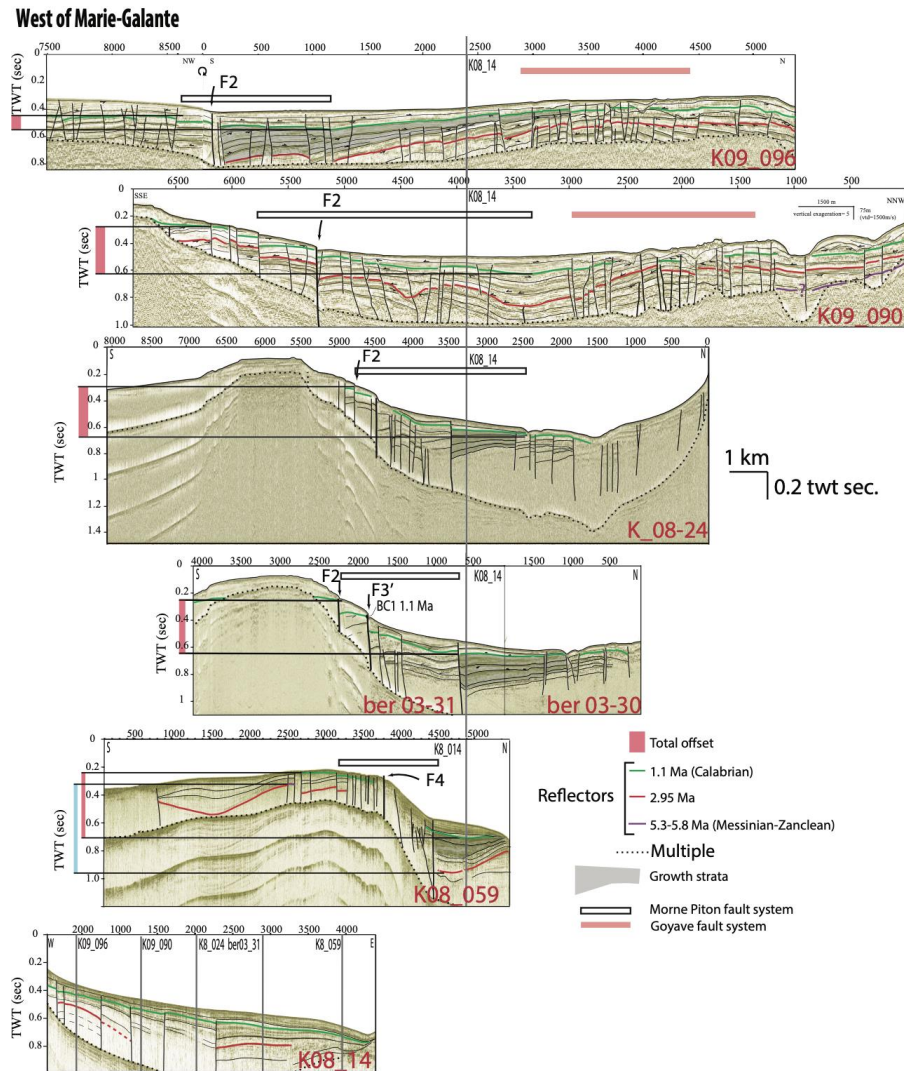
1195 Figure 2. The Marie-Galante Basin A) structural pattern after Feuillet et al. (2002) and De  
1196 Min et al. (2015) on the shaded-relief bathymetric map. blue hexagons : tide gauges  
1197 <http://refmar.shom.fr/fr/liste-maregraphes-data.shom.fr>. Red colors scale: Guadeloupe  
1198 population density per km2 after GEOFLA (<https://www.data.gouv.fr/fr/datasets/geofla-r/>). B) Sismostratigraphic scheme of the Marie-Galante basin modified after Cornée et al.,  
1200 2023. C) Colored dots: Crustal seismicity (from IRIS seismic database 2023) for magnitude  
1201 earthquakes (EQ)  $3 > M_w > 6.5$  and located from 0 to 30 km depth), red line locates the WAS  
1202 line (Kopp et al., 2011). D) Focal mechanisms solutions are indicated by red beachballs after  
1203 Gonzalez et al. (2017). The location of historical earthquakes is indicated by black stars  
1204 (after: Feuillet et al., 2011b). AP, PdC, PAP, PT stand for Anse Piton, Pointe des Chateaux,  
1205 Pointe-à-Pitre and Petite Terre.

1206



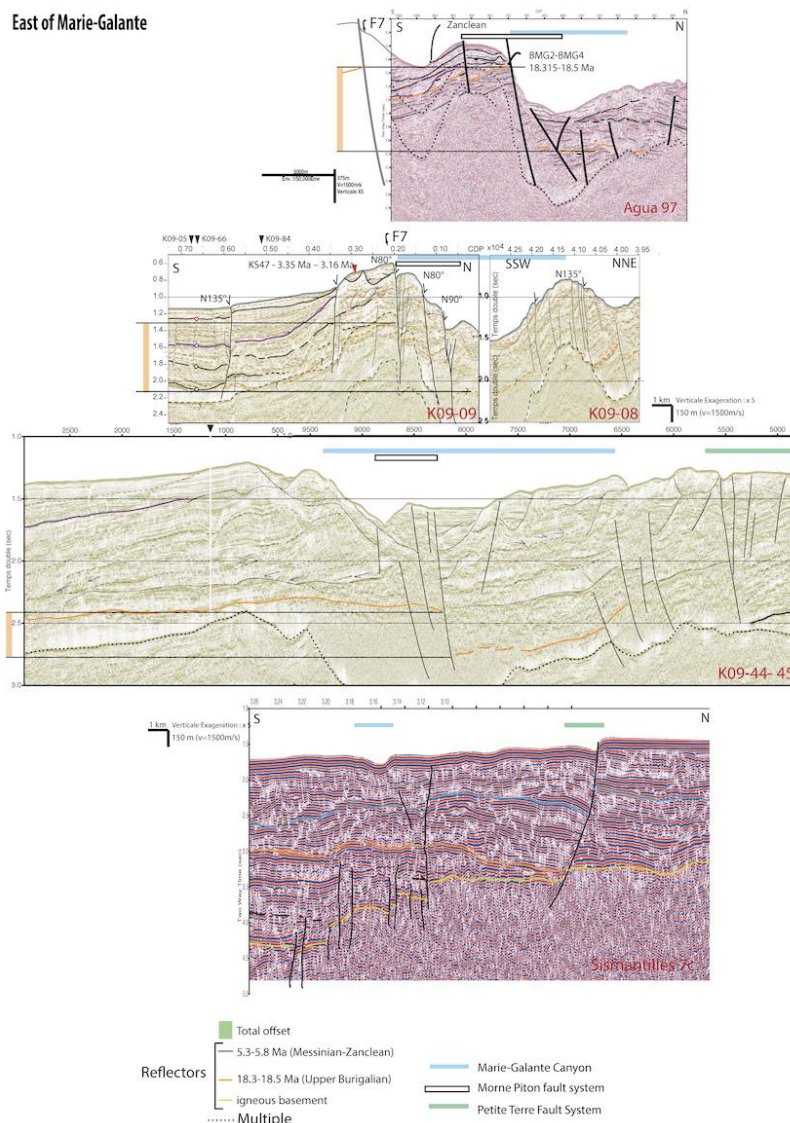
1207  
 1208 *Figure 3. A) High resolution (25m grid spacing) bathymetric map [UMO16] of the Marie-*  
 1209 *Galante Basin, offshore Guadeloupe and location of the seismic profiles shown on figures 4*  
 1210 *and 5, and location of dredge samples used for the seismic units age calibration (Münch et*  
 1211 *al. 2013). B) Structural interpretation of the E-W trending Morne Piton Fault system. C) A*  
 1212 *proxy for cumulative strain given by the graphic displaying the D (fault surface*  
 1213 *displacement) taken as the difference between the top and the toe of the fault scarp versus*  
 1214 *L (fault length) along the whole system.*





1215

1216 *Figure 4: Seismic lines West of Marie-Galante (location on Figure 3) showing the correlation*  
 1217 *across the Morne Piton Fault system of the 1.29Ma unit reflector (Green) that correspond to*  
 1218 *the reflector dredged at BC1 and BC2 location along the Ber03\_30-31 seismic line. The*  
 1219 *2.95Ma Unit Boundary (Red) is correlated from seismic lines south of the Colombie Bank*  
 1220 *and Eastern Marie-Galante Basin (line K09\_90 and K09\_26-62 location on figure 2). Notice*  
 1221 *that the basin sedimentary slope is in the E-W direction (parallel to line K08-14). Therefore,*  
 1222 *the initial topography of the reflectors in the N-S direction, across the fault system, can be*  
 1223 *neglected when measuring the offset along the seismic lines.*

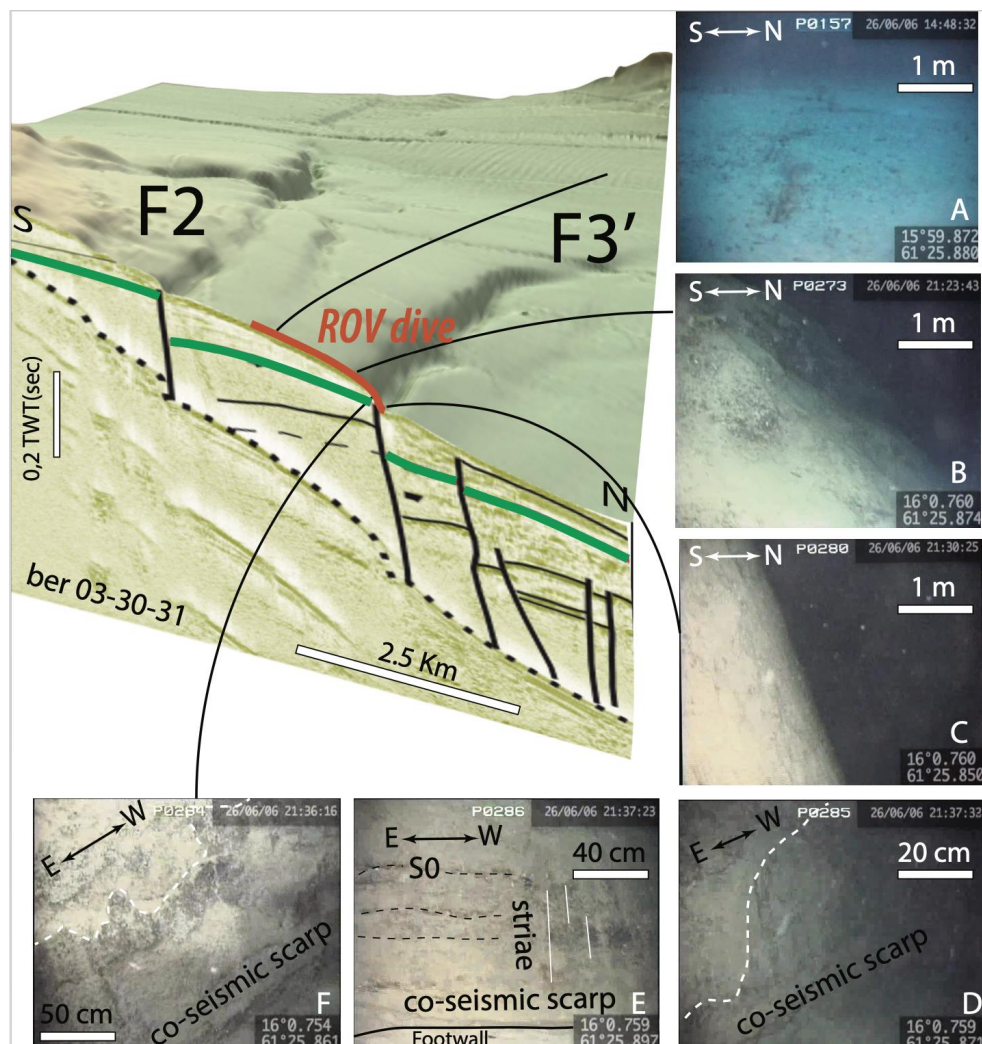


1224

1225 *Figure 5: Seismic lines east of Marie-Galante illustrate the correlation across the Morne*  
 1226 *Piton Fault system of the 7 Ma (Tortonian/Messinian) MG-SB3 sequence boundary (Purple)*  
 1227 *and the 16 Ma, (Burdigalian) MG-SB2 Sequence Boundary (Orange). Seismic line location*  
 1228 *on Figure 3).*



1229



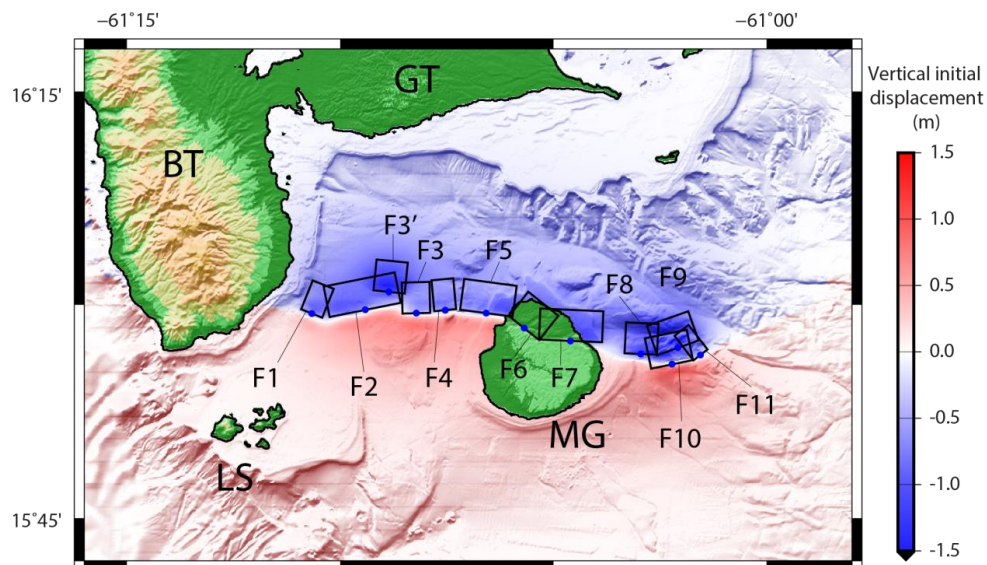
1230

1231 *Figure 6: ROV photographs of fault identified on the seafloor along the BER03-30-31 seismic*  
 1232 *line across the F3' Morne Piton Fault segment (location on Figure 3) . (A) photograph of*  
 1233 *the hangingwall of F3'. The eroded F3' fault plane presents a progressive downward slope*  
 1234 *steepening (B and C) until the toe of the fault, which is marked by a characteristic co-seismic*  
 1235 *scarp with a dip slip striae (D E F). On each photograph, white numbers starting with a P is*  
 1236 *the water depth in meters Latitude is North and Longitude is West (WGS84). A B and C*  
 1237 *views show several tens square meters wide areas, D E F are close up showing ca 1m high*  
 1238 *escarpment just above the foot of the fault scarp (visible at the bottom of each photos).*





1239

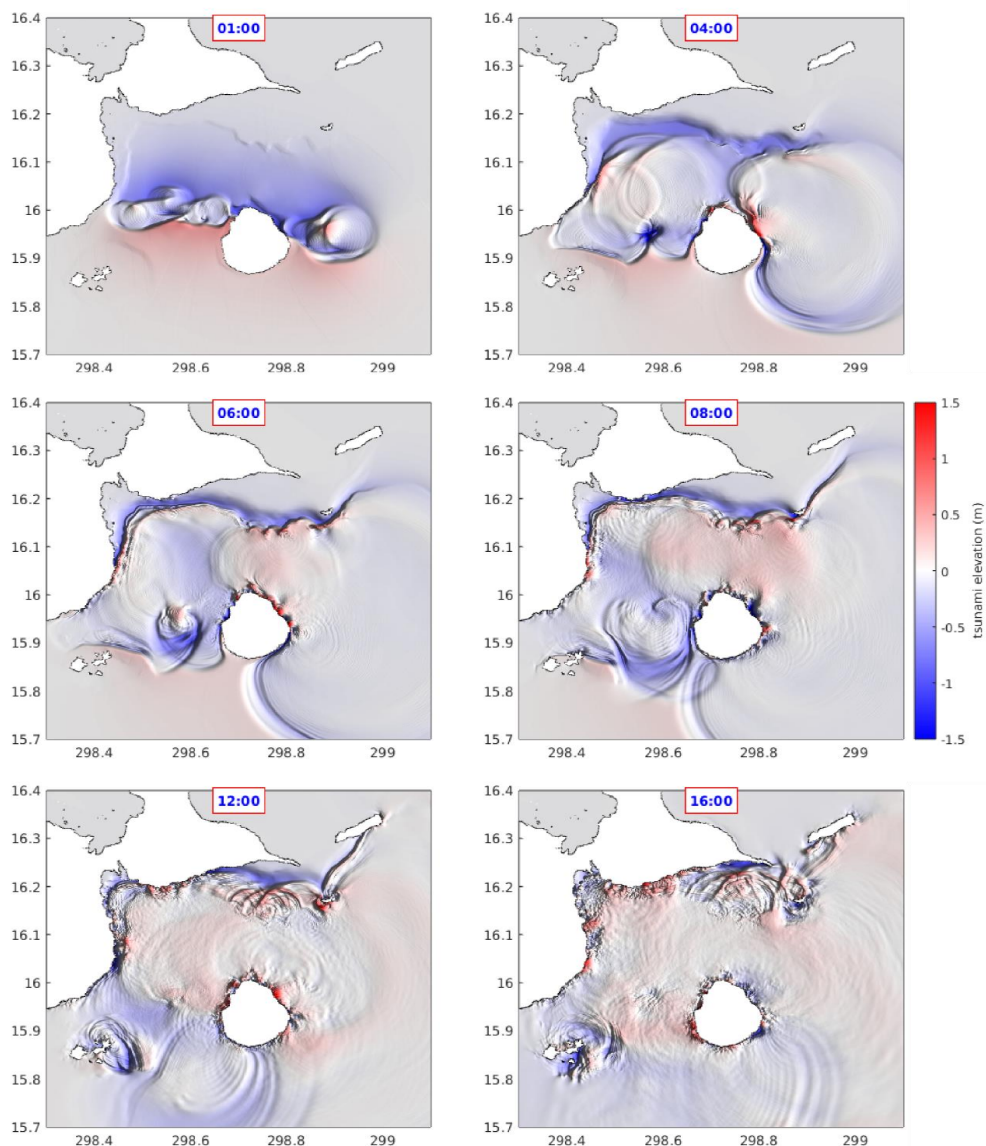


1240

1241 *Figure 7: Initial surface elevation for a maximum credible scenario built with the 11 fault*  
1242 *segments detailed in Table 3. Blue dots indicate the top fault center. Acronyms stand for*  
1243 *Grande-Terre (GT), Basse-Terre (BT), Les Saintes (LS) and Marie-Galante (MG).*



1244



1245

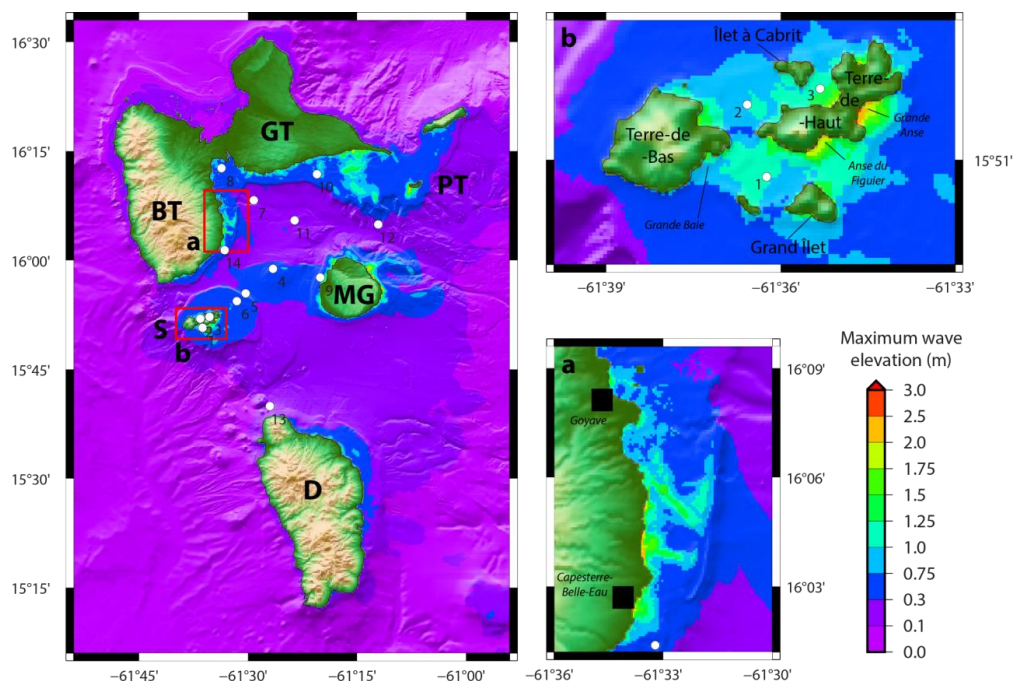
1246 *Figure 8: Snapshots of tsunami elevation within the Guadeloupe Archipelago at 1, 4, 8, 6, 12*

1247 *and 16 minutes of waves propagation. Red and blue colors correspond to wave crests and*

1248 *troughs respectively. The black arrow shows the Banc Colombie shoal. BT: Basse-Terre; GT:*

1249 *Grande-Terre; S: Les Saintes; PT : Petite-Terre ; MG : Marie-Galante.*

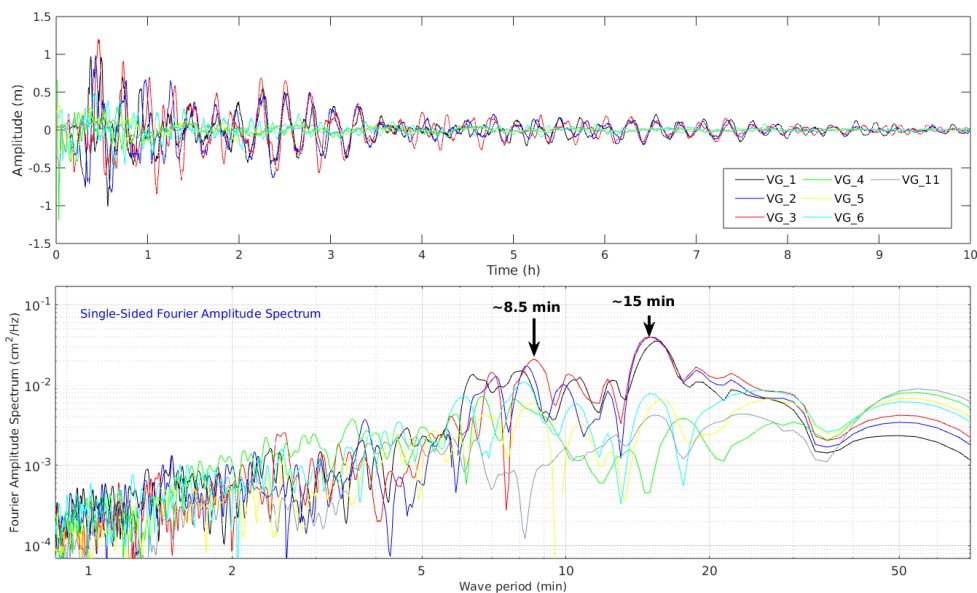
1250



1251  
 1252 *Figure 9: Shadowed bathymetric map with tsunami maximum wave elevation. Numbered*  
 1253 *white dots: fourteen virtual sea-level gauges (VG) : . BT: Basse-Terre; GT: Grande-Terre; S:*  
 1254 *Les Saintes; PT : Petite-Terre ; MG : Marie-Galante ; D : Dominica. VG\_4 & VG\_11 are located*  
 1255 *near the fault rupture region, the VG\_5 & VG\_6 are near the Les Saintes Faultsystem. VG\_1,*  
 1256 *VG\_2 & VG\_3 are within the Les Saintes archipelago.*

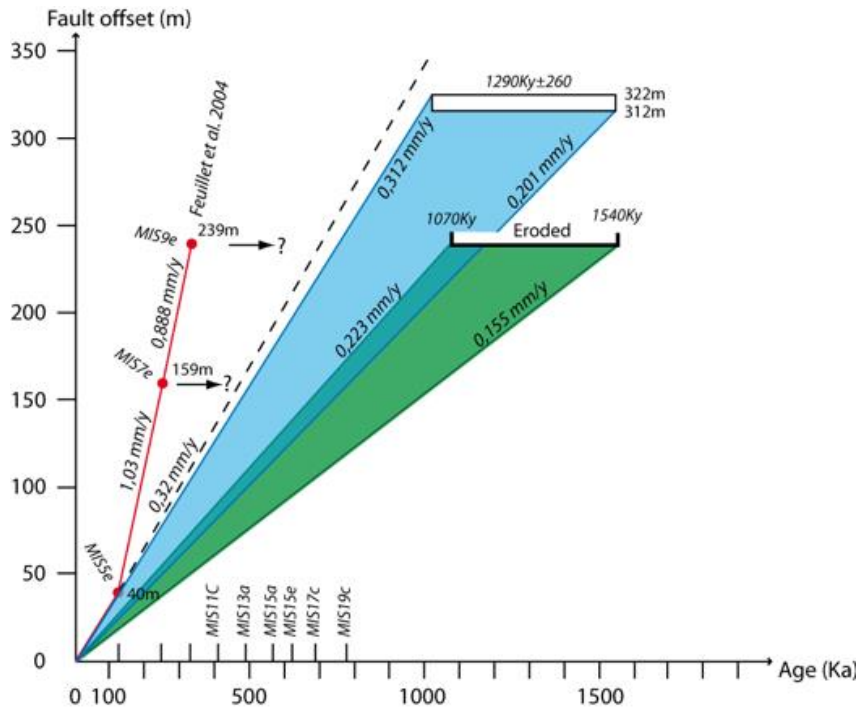


1257



1258

1259 *Figure 10: Post-processing of virtual gauge records. Top: sea-level records at 7 different*  
1260 *locations (VG 1 to 6 and VG11 – location on figure 9); bottom: single-sided Fourier*  
1261 *amplitude spectrum. The blue arrows symbolize the location of the 2 peaks of period ~6.5*  
1262 *and 17 min.*



1263  
 1264 Figure 11: Fault offset along the Morne Piton Fault against the age of the strain marker.  
 1265 Red: data from Feuillet et al. (2004) based on absolute age of terrace T4 (MIS5e), the  
 1266 estimated age of terrace T2 (MIS7e) and the suggested age of Marie-Galante upper plateau  
 1267 (MIS9e). Green: strain range calculated using upper plateau unit age from Münch et al.  
 1268 (note that erosion may lower this estimation strain rate). Blue: strain range calculated from  
 1269 the fault offset of the seismic unit dated ca 1,2Ma along the seismic line K08-59 (green  
 1270 reflector on Figure 4). Dotted line indicates the 0.32 mm.yr<sup>-1</sup> strain rate from the estimated  
 1271 offset of the MIS5e Terrace in Marie-Galante (Feuillet et al. 2004).  
 1272



Cruise	KaShallow 1	KaShallow 2	Aguadomar	SismAntilles	GEOBERYX05 SISM BGM FI35 20030000010
Seismic source	1000 J sparker	35-45 in3 GI Airguns array	45-105 in3 Two GI Airguns	4400 in3 Airguns array.	Sparker (SIG1000)
Peak frequency (far field)	250-400Hz	40-70Hz	30-50Hz	15-20Hz	100-1400Hz
Number of traces	6 traces	72 traces	6 traces	360 traces	6 traces
Fold coverage	3/6 fold	9/18 fold	3 fold	30 fold	3/6 fold
Inter CDP distance	4 m	3.125 m	4 m	6,25 m	4 m

1273

1274 *Table 1: Main acquisition parameters of the seismic data shown in this study (Figures 4 and*  
 1275 *5).*

Profiles	Age	error (Ma)	V in m/s												vertical slip rate (mm/yr)			
			horizon depth in the footwall (stwt)		horizon depth in the hangingwall (stwt)		2500		2000		2500		2000		min	max	Mean	uncertainty
			water	rock	water	rock	horizon depth in the footwall (m)	horizon depth in the hangingwall (m)	horizon depth in the footwall (m)	horizon depth in the hangingwall (m)	TOTAL OFFSET (m)	TOTAL OFFSET (m)						
K09-44-45	16	1	3.16	1.74	3.17	2.45	4545	5440	4110	4828	895	717.5	0.04	0.06	0.05	0.01		
Since fault initiation	7	1.5	3.16	1.74	3.17	2.45	4545	5440	4110	4828	895	717.5	0.08	0.16	0.12	0.06		
K09-09-08	16	1	0.6	0.71	1.27	0.85	1330	2013.8	1153.3	1802	683.8	648.3	0.04	0.05	0.04	0.01		
Since fault initiation	7	1.5	0.6	0.71	1.27	0.85	1330	2013.8	1153.3	1802	683.8	648.3	0.08	0.12	0.10	0.03		
Agu97	16	1	0.56	0.15	1.36	0.57	607.5	1732.5	570	1590	1125	1020	0.06	0.08	0.07	0.01		
Since fault initiation	7	1.5	0.56	0.15	1.36	0.57	607.5	1732.5	570	1590	1125	1020	0.12	0.20	0.16	0.06		
K08-059	1.3	0.26	0.22	0.02	0.5	0.11	190	512.5	185	485	322.5	300	0.19	0.31	0.25	0.08		
ber03-31	1.3	0.26	0.21	0.04	0.53	0.1	207.5	522.5	197.5	497.5	315	300	0.19	0.31	0.25	0.08		
K08-24	1.3	0.26	0.25	0.04	0.6	0.03	237.5	487.5	227.5	480	250	252.5	0.16	0.24	0.20	0.06		
K09-090	1.3	0.26	0.33	0.02	0.49	0.13	272.5	530	267.5	497.5	257.5	230	0.15	0.25	0.20	0.07		
K09-096	1.3	0.26	0.32	0.12	0.44	0.14	390	505	360	470	115	110	0.07	0.11	0.09	0.03		

1276

1277 *Table 2: Measured offset of seismic reflectors across the Morne Piton Fault system and*  
 1278 *calculated total vertical strain rates. See text for the ages estimate. Seismic reflectors depth*  
 1279 *on each side of the fault system is measured in time (stwt – second two way time) and*  
 1280 *converted in depth in using water velocity (1500m/s) and two end-member velocities for*  
 1281 *the sediment (see text for explanation), providing a minimum and a maximum offset value.*  
 1282 *The minimum strain rate is obtained from the ratio between the min offset and the max age*  
 1283 *bound of the reflector and vice versa.*





Fault segment	Lon (°)	Lat (°)	Length (m)	Width (m)	Top of the fault plane depth (m)	Strike (°)	Dip (°)	Rake (°)	Slip (m)
F1	-61.5335	15.98987	2838	2500	500	111.8173	75	-90	1.89
F2	-61.4708	15.994	9070	2500	500	78.6779	75	-90	1.89
F3'	-61.4428	16.01503	3918	2500	500	95.7894	75	-90	1.89
F3	-61.4108	15.99009	3474	2500	500	88.6124	75	-90	1.89
F4	-61.377	15.99367	2735	2500	500	84.8173	75	-90	1.89
F5	-61.3287	15.99021	6623	2500	500	97.5553	75	-90	1.89
F6	-61.2846	15.97275	4813	2500	500	128.5318	75	-90	1.89
F7	-61.2301	15.95767	7904	2500	500	92.4558	75	-90	1.89
F8	-61.1477	15.94221	4052	2500	500	92.8432	75	-90	1.89
F9	-61.1042	15.94958	5495	2500	500	70.5514	75	-90	1.89
F10	-61.111	15.93014	5336	2500	500	78.3772	75	-90	1.89
F11	-61.0777	15.94126	2228	2500	500	52.205	75	-90	1.89

1284

1285 *Table 3: Parameters used for the tsunami source simulation of a rupture along the*  
 1286 *multisegment fault presented in figure 7.*

1287